OULUN YLIOPISTO
UNIVERSITY of OULU

DEPARTMENT OF MECHANICAL ENGINEERING

CERN-THESIS-2013-120
/ /2013

THERMO-MECHANICAL MODELLING AND EXPERIMENTAL VALIDATION OF CLIC PROTOTYPE MODULE TYPE 0

Lauri Kortelainen

Master's Thesis

Supervisors:
Dr. Ivan Argatov
Dr. Hannu Koivurova
Dr. Germana Riddone
Dr. Kenneth Österberg

TIIVISTELMÄ

Thermo-mechanical modelling and experimental validation of CLIC prototype module type 0

Lauri Kortelainen

Oulun yliopisto, Konetekniikan osasto

Diplomityö 2013, 77 s.

Työn ohjaajat:
Dr. Ivan Argatov
Dr. Hannu Koivurova
Dr. Germana Riddone
Dr. Kenneth Österberg

Suunnitteilla olevan seuraavan sukupolven lineaarisen hiukkaskiihdyttimen 48.3 kilometrin pituus koostuu kaksimetrisistä moduuleista. Lämpöhäviöt komponenteissa johtavat moduulin lämpötilan nousuun ja sitä kautta muodonmuutoksiin. Moduuleita on voitava stabiloida mikrometrien tarkkuudella tarvittavan luminositeetin saavuttamiseksi. Ensimmäinen CLIC-prototyyppimoduuli on kokoonpantu CERNissä ja testiohjelma, jonka tarkoituksena on tutkia sen lämpökäyttäytymistä oikeata rakennetta vastaavissa käyttöolosuhteissa on aloitettu.

Tässä diplomityössä on mallinnettu ensimmäistä CLIC-prototyyppimoduulia käyttäen elementtimenetelmää. Mallinnuksen tavoitteena on ollut arvioida rakenteen lämpötilajakaumaa sekä lämpötilan muutoksesta aiheutuvia muodonmuutoksia testiohjelman mukaisissa käyttöolosuhteissa. Numeerisia tuloksia on verrattu kokeellisiin tuloksiin ja on huomattu, että ne vastaavat toisiaan hyvin sekä lämpökäyttäytymisen että muodonmuutosten osalta.

Asiasanat: CERN, CLIC, FEA

ABSTRACT

Thermo-mechanical modelling and experimental validation of CLIC prototype module type 0

Lauri Kortelainen

University of Oulu, Department of Mechanical Engineering

Master's thesis 2013, 77 p.

Supervisors:
Dr. Ivan Argatov
Dr. Hannu Koivurova
Dr. Germana Riddone
Dr. Kenneth Österberg

Micron level stability of the two-meter repetitive modules constituting the two main linacs is one of the most important requirements to achieve the luminosity goal for the Compact Linear Collider. Structural deformations due to thermal loads and related to the RF power dissipated inside the modules affect the alignment of the linacs and therefore the resulting luminosity performance. A CLIC prototype module has been assembled in a dedicated laboratory and a thermal test program has been started in order to study its thermo-mechanical behaviour.

This thesis focuses on the finite elements modelling of the first CLIC prototype module 0. The aim of the modelling is to examine the temperature distributions and the resulting deformations of the module in different operating conditions defined in the thermal test program. The theoretical results have been compared to the experimental ones; the comparison shows that the results are in good agreement both for the thermal behaviour of the module and for the resulting misalignments due to thermal expansion.

Keywords: CERN, CLIC, FEA

FOREWORDS

This thesis was carried out at CERN in a collaboration with Helsinki Institute of Physics (HIP) and University of Oulu. I would like to thank my supervisors Dr. Ivan Argatov, Dr. Hannu Koivurova, Dr. Germana Riddone and Dr. Kenneth Österberg for their guidance and support. I also thank Dr. Fabrizio Rossi for giving me technical advice during the development of the simulation.

Geneva, 14th of August, 2013

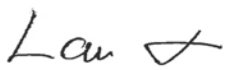

Lauri Kortelainen

TABLE OF CONTENTS

ABBREVIATIONS

AS	Accelerating Structure
ASL	Accelerating Structure Load
CATIA	Computer Aided Three-dimensional Interactive Application
CL	Compact Load
CLIC	Compact Linear Collider
CMF	Choke Mode Flange
DBQ	Drive Beam Quadrupole
LEP	Large Electron-Positron Collider
LHC	Large Hadron Collider
PETS	Power Extraction and Transfer Structure
PETSu	PETS unit
RFN	RF Network
RFNL	RF Network Load
SAS	Super Accelerating Structure
TS	Temperature Sensor
WG	Waveguide

NOTATIONS

A	Surface area
c_p	Specific heat
$\dot{E}_{in}$	Energy entering system
$\dot{E}_{out}$	Energy leaving system
h	Heat transfer coefficient
h_a	Heat transfer coefficient to air
h_w	Heat transfer coefficient to water
k	Conductivity
L	Length
L_c	Characteristic length
$\dot{m}$	Mass flow rate
Nu	Nusselt number
Pr	Prandtl number
$\dot{Q}$	Heat power
$\dot{q}$	Heat generation
Re	Reynold’s number

Re_{xc}	Critical Reynold's number
T	Temperature
T_i	Inlet temperature
T_o	Outlet temperature
T_s	Surface temperature
T_∞	Ambient temperature
t	Time
u	Flow speed
u_∞	Air speed
$\dot{V}$	Volumetric flow rate
x,y,z	Cartesian coordinates

ε	Emissivity
μ	Dynamic viscosity
ρ	Density
σ	Stefan-Boltzmann constant

1 INTRODUCTION

Micron level stability of the two-meter repetitive modules constituting the two main linacs is one of the most important requirements to achieve the luminosity goal for the Compact Linear Collider. Structural deformations due to thermal loads and related to the RF power dissipated inside the modules affect the alignment of the linacs and therefore the resulting luminosity performance.

This thesis presents the finite element modelling of the CLIC prototype module type 0. The aim of the modelling is to examine the temperature distributions and the resulting deformations of the module in different operating conditions. In parallel CLIC prototype module type 0 has been assembled in a dedicated laboratory at CERN and a thermal test program has been started to study its thermo-mechanical behaviour. The experimental data obtained from the tests are used to validate the theoretical results of the finite elements simulation. In addition, theoretical background on heat transfer is presented.

Chapter 1 introduces CERN and CLIC project. The CLIC prototype module type 0 and its components are presented in chapter 2. Chapter 3 presents theoretical background on heat transfer while chapter 4 describes the finite element model created in detail. The thermal test program is described in chapter 5 and the results from the finite element simulation and comparison to the experimental data are presented in chapter 6. Finally, the results and future steps are discussed in chapter 7.

1.1 Background

The European Organization for Nuclear Research (CERN), one of the world’s largest and most respected particle physics laboratory, was founded in 1954. Today CERN is run by 20 Member States but also many non-European countries are involved in different research programs. (Ellis 2000.) Currently about 2400 people are employed by CERN but over 10 000 visiting scientists are related to the on-going projects through their research. They represent 608 universities and 113 nationalities. (About CERN 2013.)

CERN's main function is to provide accelerators for the high-energy physics research. During CERN's existence, several important scientific discoveries have been made in physics. Furthermore, the research work related to particle accelerator studies has revolutionized the technology used in many other fields. For example, CERN had an important role in the discovery of Positron Emission Tomography (PET) technology, which enables three-dimensional imaging of the functional processes of the brain. Recently, CERN has been a centre for the development of the grid network which enables the handling of large amounts of data produced by the current accelerator projects. (Physics for Health 2010.)

At the moment, LHC (Large Hadron Collider), which was completed in 2008, is CERN's most important accelerator. The circular LHC tunnel, which was occupied by LEP (Large Electron-Positron Collider) until year 2000, has a circumference of 27 km and is located 100 meters underground. On the 4th of July 2012 CERN held a press conference in which the finding of a new gauge boson was confirmed. As of February 2013 the operation of LHC was interrupted for LS1 (Long Shutdown 1). During shutdown wear parts will be replaced and upgrades will be made.

Many of the open questions in physics can be best addressed by a lepton-antilepton (electron-positron collider) instead of a hadron collider like LHC. A consensus has been reached among particle physicists that the results from the LHC have to be complemented by experiments at an electron-positron collider operating in the TeV energy range. (Ellis 2000: 3.) Today, two approaches as a future linear collider are being developed in parallel: International Linear Collider (ILC) and Compact Linear Collider (CLIC). They have a different energy range, which leads to a different choice of technology. The main difference between the two is that ILC uses superconducting technology like LHC, which means components must be close to the absolute zero temperature, while CLIC uses normal-conducting technology at temperatures close to room temperature. (Geschonke 2010.)

1.2 CLIC study

The CLIC study has proven the feasibility of a multi TeV linear electron-positron collider with an accelerating gradient of 100 MV/m. The current CLIC layout is presented in Figure 1. (Stapnes et al. 2012)

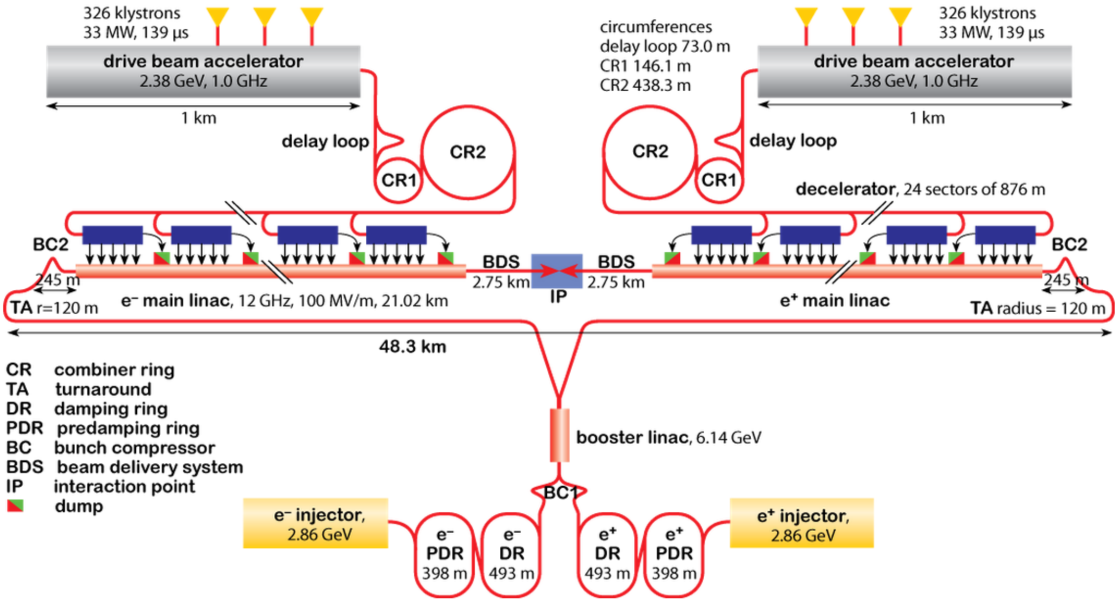

Figure 1. The proposed layout for CLIC.

The layout of CLIC relies on transforming the high current intensity and low energy from the Drive Beam (DB) to the low current and high energy Main Beam (MB). The RF power created in Power Extraction and Transfer Structures (PETS) is transferred through RF network to the Accelerating Structures (AS). The beam focusing is achieved by using quadrupole magnets (DBQ) which are situated along the whole length of the linac. The concept of the accelerator with the main components such as AS, PETS and DBQs can be seen in Figure 2. (Stapnes et al. 2012)

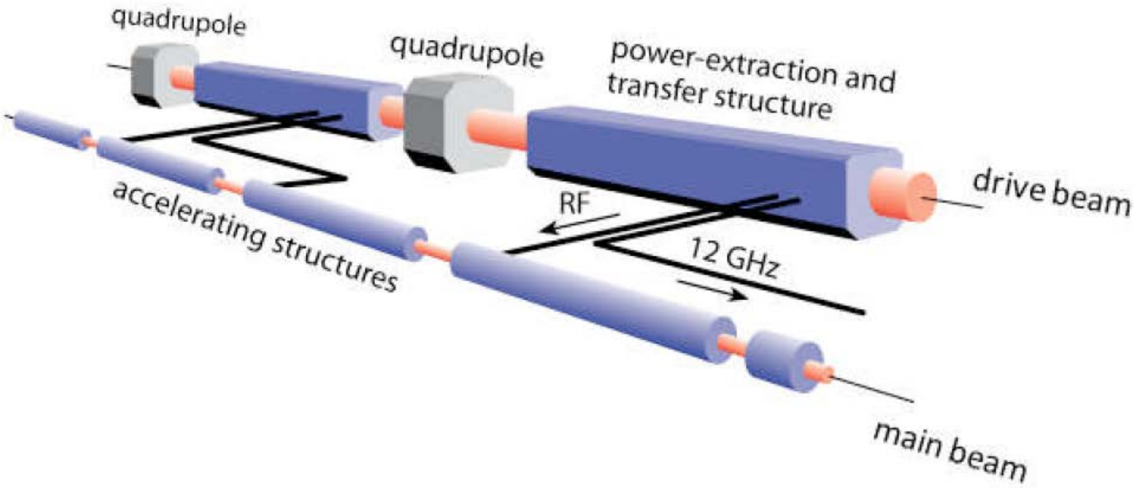

Figure 2. The CLIC Two-Beam scheme. The power provided by PETS is transferred to AS through RF network.

2 CLIC PROTOTYPE MODULE TYPE 0

CLIC prototype module type 0 has been assembled in a dedicated laboratory (Figure 3). A thermal test program has been started in order to understand its thermo-mechanical behaviour in different operating conditions.

The temperature of the module rises due to the heat generated in the RF structures. This leads to the misalignment of the module due to thermal expansion. The baseline values of the nominal heat powers for different components are presented in Table 1.

The module is cooled with water cooling channels. The baseline values of the cooling channels properties are shown in Table 2. An air conditioning and ventilation system has been installed in the laboratory to reproduce the same temperature and air speed conditions as in the CLIC tunnel. Some of the heat generated in the module is transferred to air from the outer surfaces of the module. The air properties during normal operating modes of CLIC modules are shown in Table 3.

Other aims of the first prototype are to show the feasibility of the proposed solutions for the different technical systems, such as supporting, pre-alignment, vacuum and cooling systems (Gudkov 2013). All the mechanical interfaces of the components and vacuum internal volumes have been kept equal to those of the real CLIC module type 0. The different components of the module are presented in this chapter.

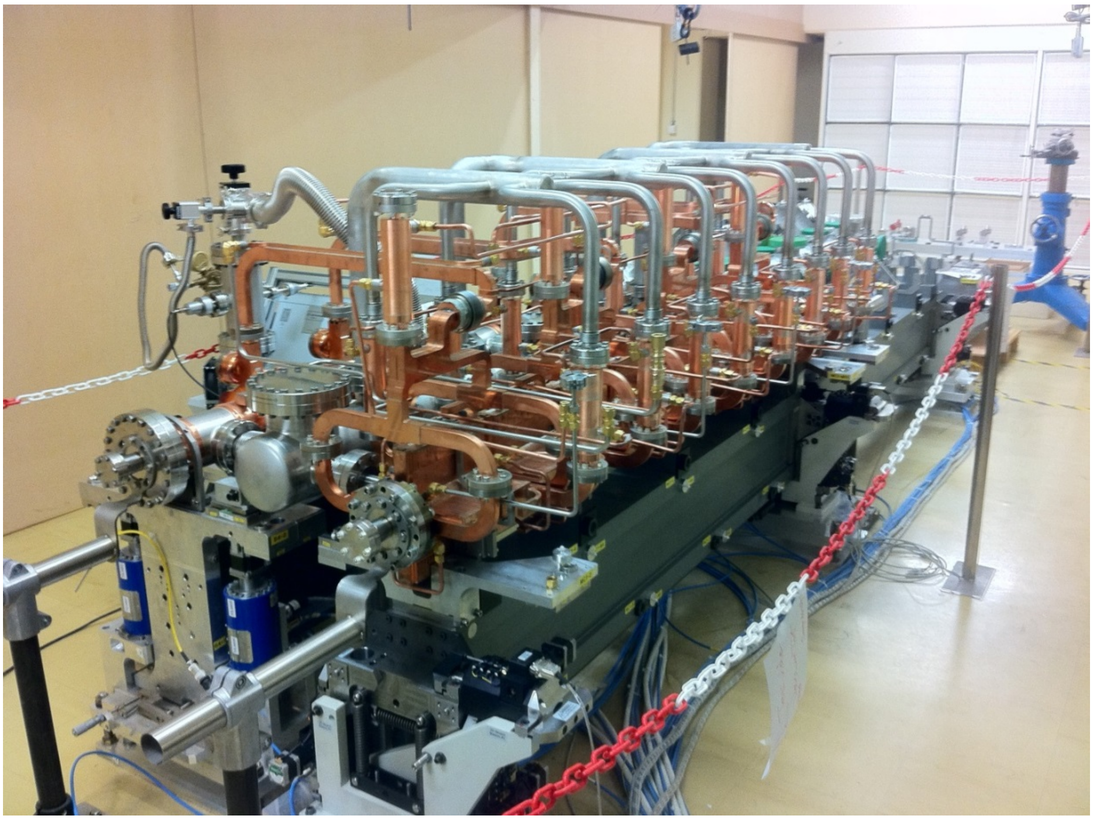

Figure 3. CLIC prototype module type 0.

Table 1. CLIC baseline nominal heat power values.

Item	**Heat power (W)**
SAS	820
PETS	110
CL	150
DBQ	150

Table 2. CLIC baseline cooling channels properties.

Property	**SAS**	**PETS**
Inlet temperature T_i (°C)	25	25
Mass flow $\dot{V}$ (m^3/h)	0.0686	0.0374

Table 3. CLIC baseline air properties.

Property	**Value**
Air speed u_∞ (m/s)	0.7
Ambient temperature T_∞ (°C)	40

2.1 Accelerating Structures

The design of CLIC Accelerating Structures (AS) is based on oxygen-free copper disks which are connected to each other by diffusion bonding with hydrogen at temperatures close to the melting temperature of the material 1083 °C. After bonding the AS disks are assembled together with other components such as vacuum manifolds, input waveguides and cooling circuits. A typical AS disk and AS assembly are shown in Figure 4. In the CLIC prototype module 0 the eight real AS have been replaced by a two meter long mock-up for which the real geometry has been simplified still maintaining the same interfaces and internal volume as in the real AS. The mock-up is shown in Figure 5.

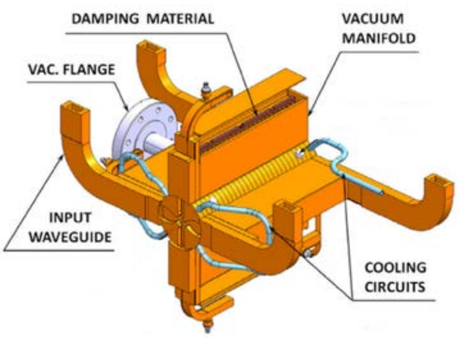

Figure 4. Left: A typical AS disk. Right: AS assembly.

Figure 5. AS mock-up.

2.2 Power Extraction and Transfer Structure

The RF power produced in the DB side is collected by means of the Power Extractor and Transfer Structure and delivered to the Accelerating Structures. In the current layout single PETS provides RF power for two AS. The real PETS are composed of copper octants separated by damping slots. The octants are jointed together and assembled with other components, such as mini-tanks and couplers into a complete PETS unit (Figure 6). The interfaces of the PETS mock-up correspond to those found in the real PETS unit. The octants have been replaced by a copper block with holes and slots still maintaining the same internal volume and surface area. The PETS unit mock-up is shown in Figure 7.

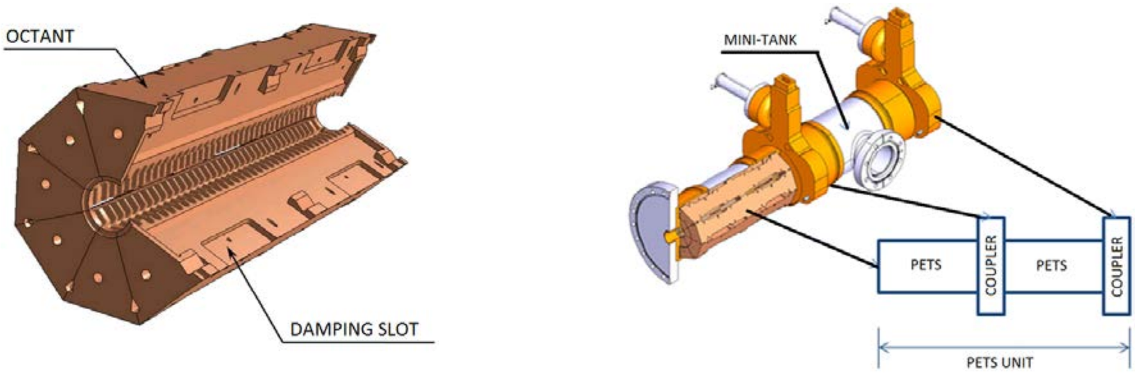

Figure 6. The octants (left) and an assembled PETS unit (right).

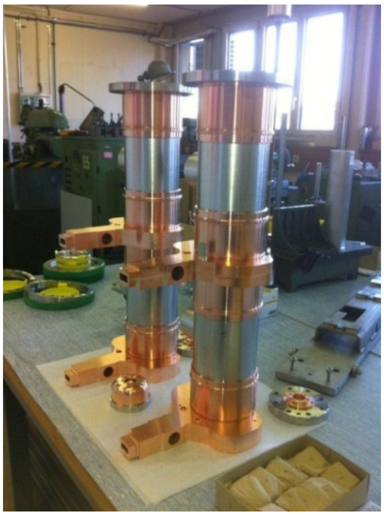

Figure 7. PETS unit mock-up.

2.3 Quadrupole Magnets

The CLIC two-beam module type 0 includes two Drive Beam Quadrupoles (DBQ), whose purpose is to keep the DB focused. The Beam Position Monitor (BPM) monitors the beam and DBQ is adjusted accordingly. In the CLIC prototype module type 0 the real DBQs have been replaced by dedicated mock-ups having the same interfaces and weight as the real ones; no cooling channels have been installed inside the mock-up DBQs. 3D model of the real DBQ and the mock-up DBQ, made of stainless steel, are shown in Figure 8.

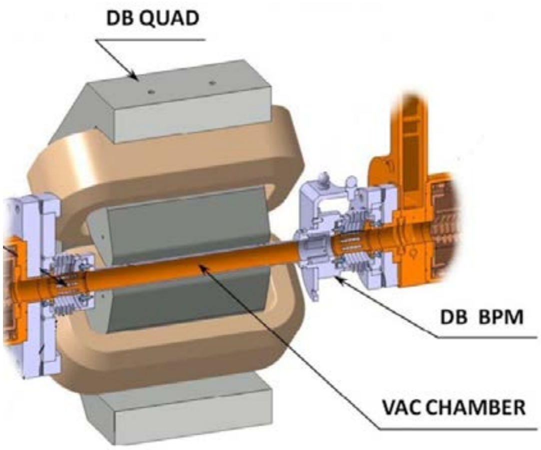

Figure 8. 3D model of the real DBQ (left) and a DBQ mock-up (right).

2.4 Vacuum System

The vacuum system for CLIC module type 0 is shown in Figure 9. Four Vacuum Networks (VN) connect the Vacuum Reservoir (VR) to the Compact Loads (CL), located on top of AS, through flexible bellows. VR is also connected to AS and PETS through flexible bellows. The required vacuum level of 10^{-9} mbar is provided by vacuum ion pump and two vacuum cartridge pumps which are installed on VR. The VR and VN for CLIC prototype module type 0 before installation are shown in Figure 10.

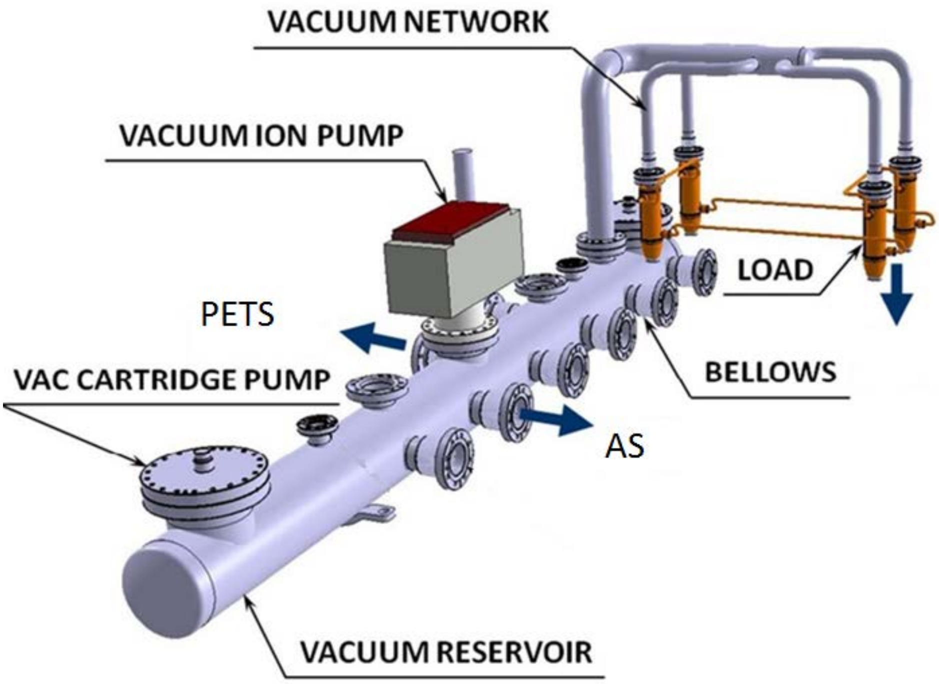

Figure 9. Vacuum system for CLIC module type 0.

(A)

(B)

Figure 10. VR (A) and VN (B) for CLIC prototype module type 0 before installation.

2.5 RF Network

The CLIC two-beam module RF network (Figure 11) consists of water cooled waveguides (WG), Choke Model Flange (CMF), RF Load and the Hybrid. The function of RF network is to transfer and distribute RF power from PETS to AS. CMF provides an electrically contact-free connection between the waveguides and permits to align DB and MB separately without introducing any RF phase errors, while the Hybrid distributes the RF power between two adjacent AS. In order to avoid RF reflection back to PETS, RF load has been attached to one of the hybrid ports to absorb RF power. RF network mock-up for CLIC prototype module type 0 before installation is shown in Figure 12.

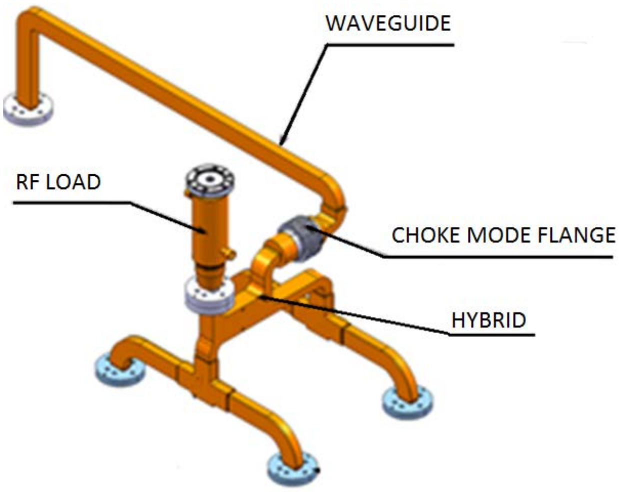

Figure 11. 3D model of RF network.

Figure 12. RF network mock-up for CLIC prototype module type 0.

2.6 Cooling System

A cooling system, made of copper cooling tubes, is integrated in the module to extract the heat generated in the components. In the current cooling scheme the water inlet temperature is 25 °C and the aim is to regulate the flow so that the outlet temperature of the water can be controlled. The cooling is based on a fully turbulent flow to ensure an efficient heat transfer. The water cooling scheme for CLIC module prototype type 0 is shown in Figure 13. DBQs are not cooled in the lab setup.

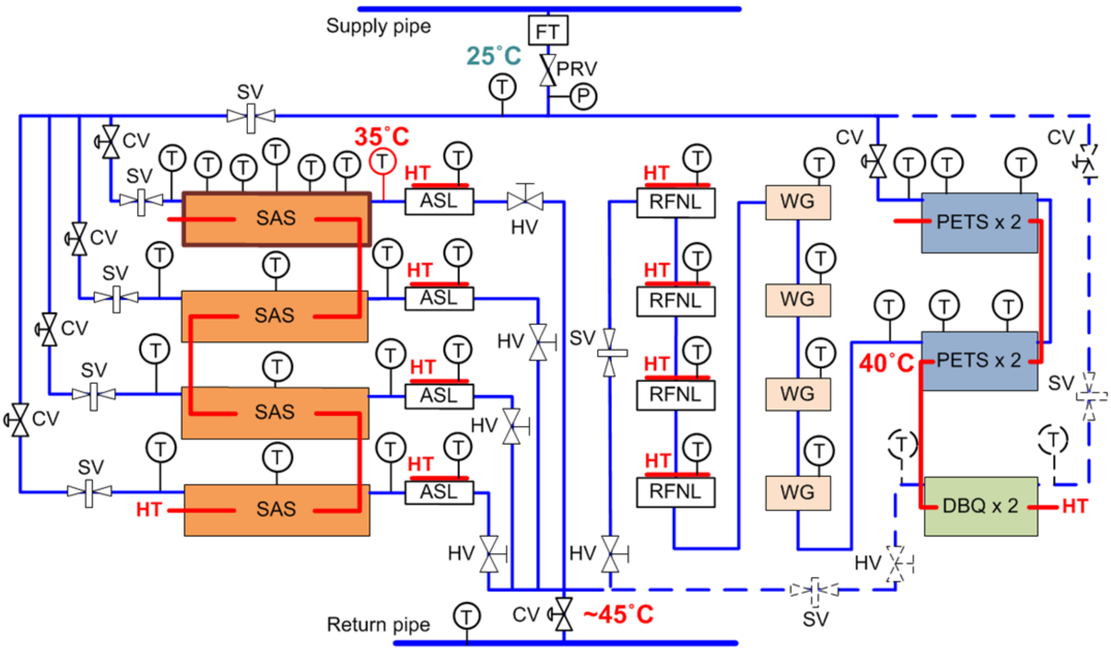

Figure 13. The cooling scheme for CLIC module prototype type 0. DBQs are not cooled.

2.7 Supporting and Alignment System

The supporting system consists of girders for MB and DB, V-shaped supports on top of the girders and cradles in the extremities of the girders. The cradles house the actuators which are used to align the girders. The supporting system is shown in Figure 14.

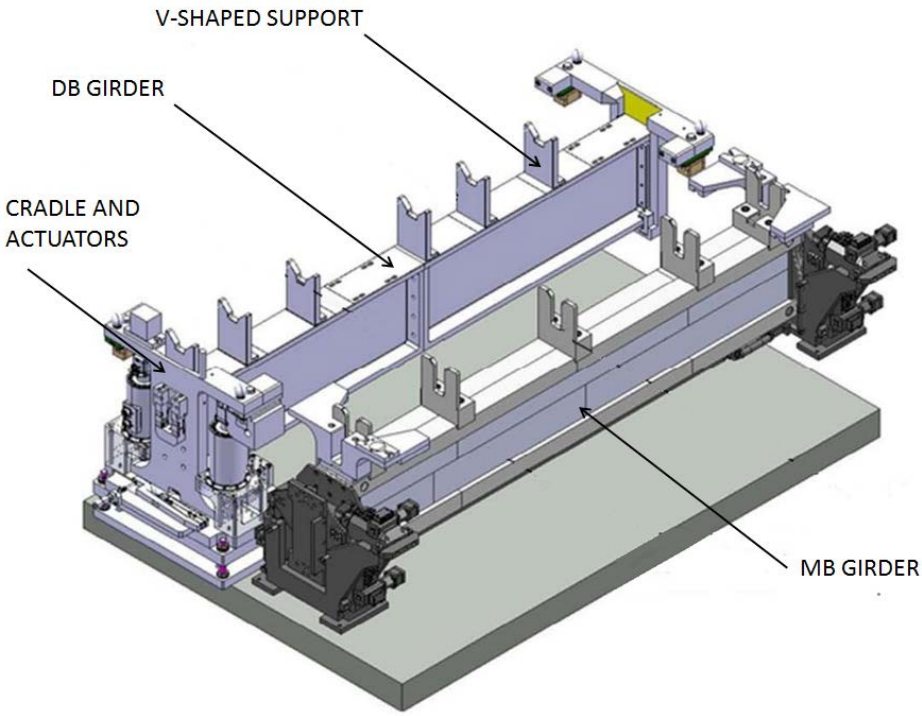

Figure 14. The supporting system for CLIC prototype module type 0.

2.7.1 Girders and V-shaped supports

The module supporting system includes two girders, one for MB and one for DB, both made of silicon carbide. MB girder is made of hollow tubes glued together to form the structure, while DB girder is made of two sections brazed together. The V-shaped supports, also made of silicon carbide, are located on top of the girders. The V-shaped supports for DB have been brazed to the girder whereas the supports for MB have been glued and screwed. The MB girder and corresponding V-shaped supports are shown in Figure 15. The V-shaped supports have to be fixed and well-positioned on the top of the girders in order to ensure the positioning of the RF structures according to the tolerance determined by physics requirements. The tolerance field, represented by a cylinder of 10 µm diameter, is shown in Figure 16.

Figure 15. MB girder and V-shaped supports for CLIC prototype module 0.

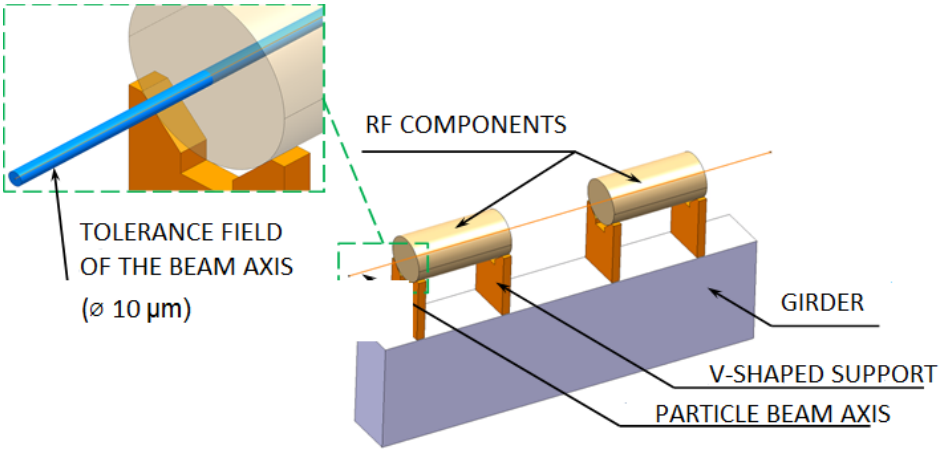

Figure 16. Tolerance field of beam axis.

2.7.2 Cradles and actuators

The girders are supported on their extremities by cradles, which are mechanically connected to the actuators. These actuators are used for repositioning of the girders. Each girder has a master and slave cradle enabling a coupled support of adjacent girders; master cradle includes two vertical and one radial actuator whereas a slave cradle is equipped with one vertical and one radial actuator. Master cradle for MB girder is shown in Figure 17.

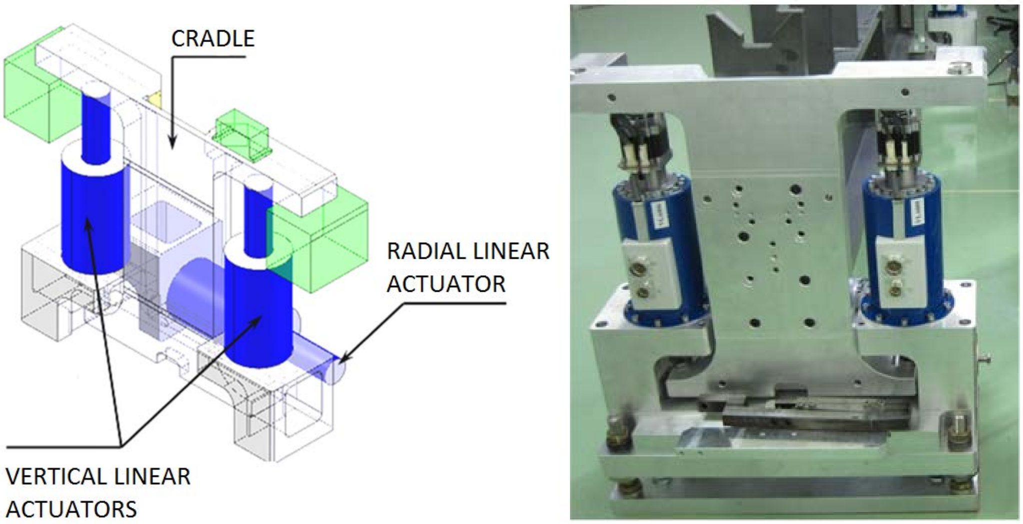

Figure 17. A master cradle and actuators for MB girder

2.8 Bellows

Bellows, shown in Figure 18, are installed in the module to decouple freedom of degrees between adjacent components, allowing for the alignment of the different parts of the module separately. Bellows connect VR to both PETS (A) and SAS (B). CMF (Choke Mode Flange) is located in RF network connecting WG to the Hybrid (C), while CL bellows connect VN to CL (D).

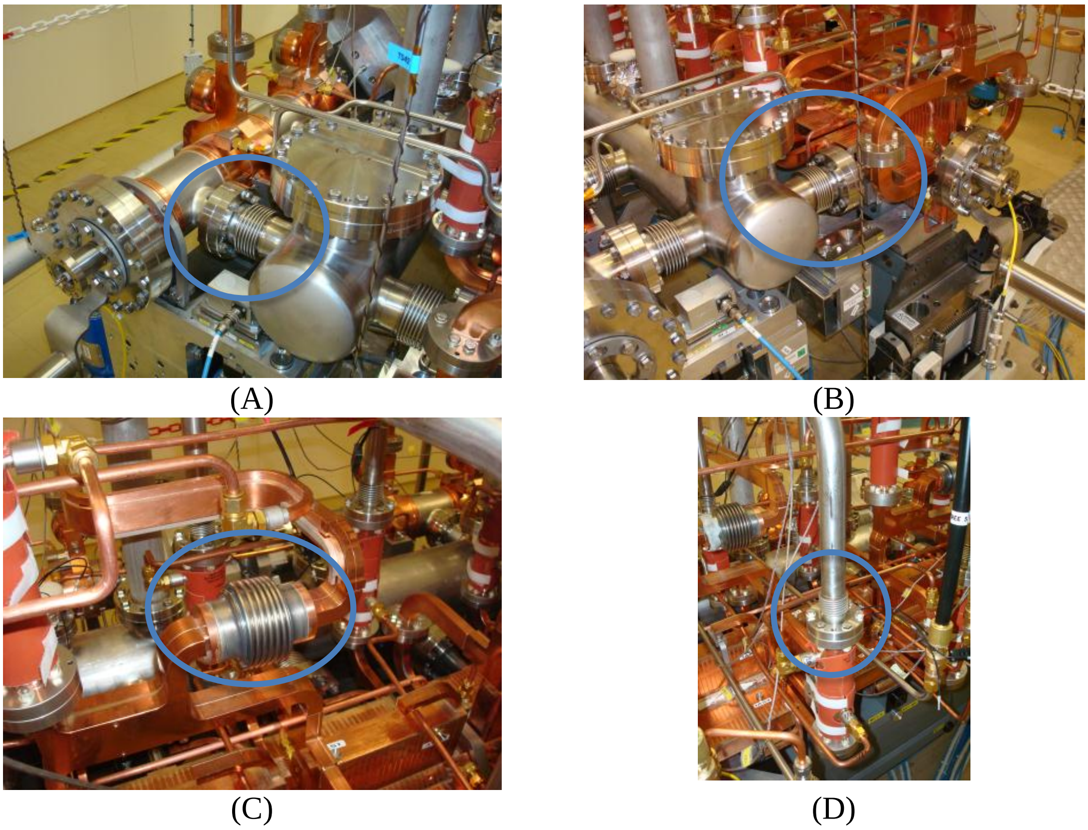

Figure 18. Bellows of CLIC prototype module type 0. PETS (A), SAS (B), CMF (C) and CL (D).

3 THEORETICAL BACKGROUND

This chapter presents theoretical background on heat transfer.

3.1 First law of thermodynamics

The first law of thermodynamics states that energy can neither be destroyed or created, it can only change forms. Conservation of energy is applied by first identifying a control volume in space. This control volume (Figure 19) is bounded by a control surface through which three forms of energy: heat, work and mass can pass.

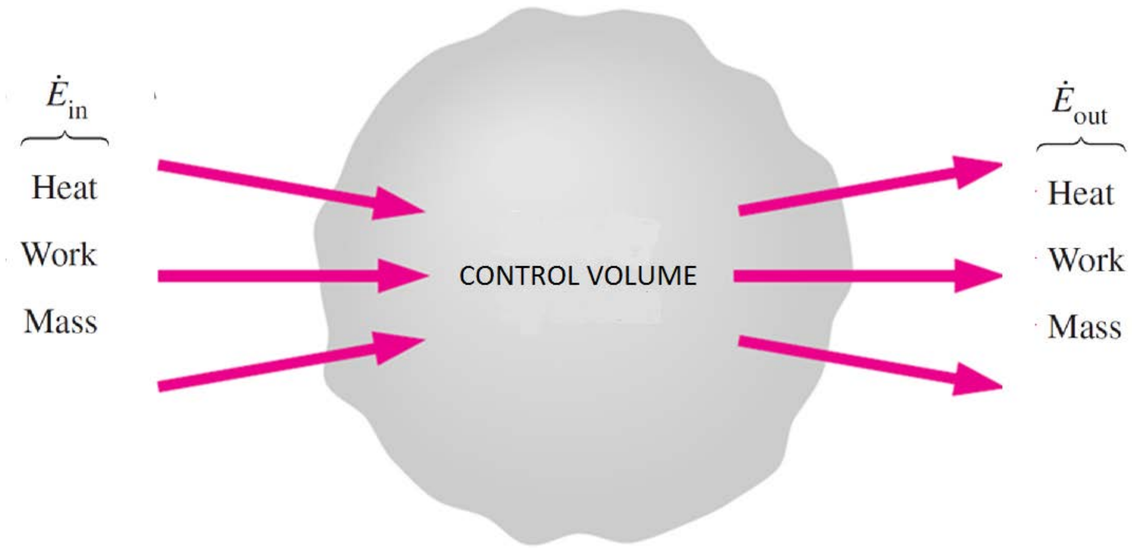

Figure 19. A control volume.

The energy balance for a control volume in rate form is expressed as

$$\dot{E}_{in} - \dot{E}_{out} = \frac{dE_{system}}{dt}, \quad (1)$$

where $\dot{E}_{in}$ is the energy going in the system, $\dot{E}_{out}$ is the energy leaving the system and dE_{system}/dt is the change in the internal energy of the system.

If the system is steady-state, the energy balance is reduced to

$$\dot{E}_{in} = \dot{E}_{out} \, . \tag{2}$$

For a one-dimensional steady flow system, the control volume is shown in Figure 20. On the basis of the principle of mass conservation, the rate of mass flow entering the system must be the same leaving it, denoted $\dot{m}$.

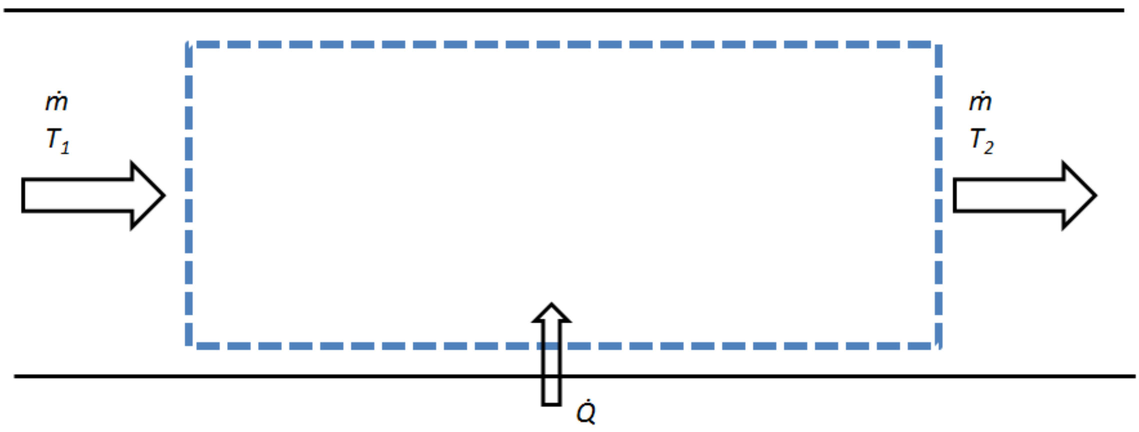

Figure 20. A 1D steady flow system with one inlet and outlet.

The energy balance for such a system, according to the first law of thermodynamics, is

$$\dot{Q} = \dot{m} c_p \Delta T, \tag{3}$$

where $\dot{Q}$ is the heat transfer rate, $\dot{m}$ is the mass flow rate, c_p is the specific heat of the fluid and ΔT is the temperature difference between the inlet and the outlet.

Heat transfer problems can be classified as either steady-state or transient. In steady-state problem the temperature is only a function of the Cartesian coordinates and independent of time, $T = T\ (x,y,z)$. In transient problem the temperature is a function of the Cartesian coordinates and time, $T = T(x,y,z,t)$.

3.2 Heat transfer mechanisms

The basic modes of heat transfer are conduction, convection and radiation. The modes are illustrated in Figure 21.

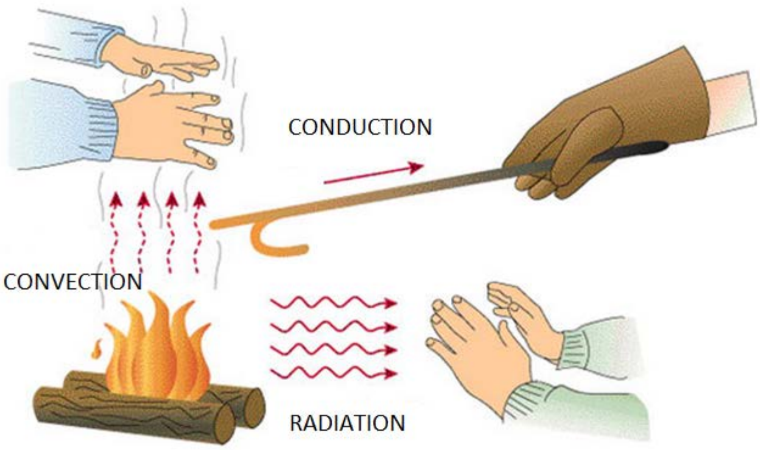

Figure 21. The basic modes of heat transfer.

3.2.1 Conduction

The transfer of heat from a higher to a lower temperature in a body or between two bodies in contact is called **conduction**. In molecular level the more energetic molecules collide with molecules of lower energy exchanging energy and momentum. Heat is conducted in two modes: 1) the flow of thermally activated electrons (conductors) or 2) lattice waves generated by thermally induced atomic activity (insulators). Fourier's law states that in conduction the heat transfer rate is proportional to the temperature gradient:

$$\dot{Q} = -kA\frac{dT}{dx}, \tag{4}$$

where *k* is conductivity, *A* is the surface area of the convection and *dT/dx* is the temperature gradient in the direction of the conduction. (Holman 2010; Kotandaraman 1998.)

Fourier's law and the first law of thermodynamics can be used as a starting point to determine a basic equation for the transfer of heat in solids called the conduction equation. For one-dimensional conduction, a control volume shown in Figure 22, with a length *dx* and a cross-sectional area *A* is used.

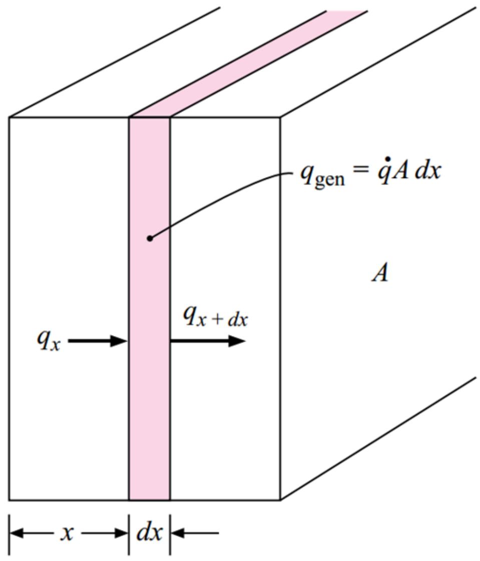

Figure 22. One-dimensional control volume with a length *dx* and cross-sectional area *A*.

According to the first law of thermodynamics, the following energy balance can be made:

energy conducted in from the left face + heat generated in the element = change in internal energy + energy conducted out from the right face

The energy balance in equation form is defined as

$$-kA\frac{\partial T}{\partial x} + \dot{q}Adx = \rho c_p A\frac{\partial T}{\partial t}dx - A[k\frac{\partial T}{\partial x} + \frac{\partial}{\partial x}\left(k\frac{\partial T}{\partial x}\right)dx], \quad (5)$$

where $\dot{q}$ is the heat generation and ρ is density. Equation 5 can be further reduced to form

$$\frac{\partial}{\partial x}\left(k\frac{\partial T}{\partial x}\right) + \dot{q} = \rho c_p \frac{\partial T}{\partial t}. \quad (6)$$

If the restriction of the temperature distribution being one-dimensional is removed and the temperature is assumed to be a function of all the Cartesian coordinates and time, $T = T(x,y,z,t)$, the conduction equation becomes

$$\frac{\partial^2 T}{\partial x^2} + \frac{\partial^2 T}{\partial y^2} + \frac{\partial^2 T}{\partial z^2} + \frac{\dot{q}}{k} = \rho c_p \frac{\partial T}{\partial t}. \quad (7)$$

3.2.2 Convection

Convection refers to the transfer of heat from a surface of a body to a fluid in motion. Convection can be either **forced convection** where the fluid motion is induced by a pump or a fan or **natural convection** where the fluid motion is a result of density difference produced by the temperature difference (Figure 23).

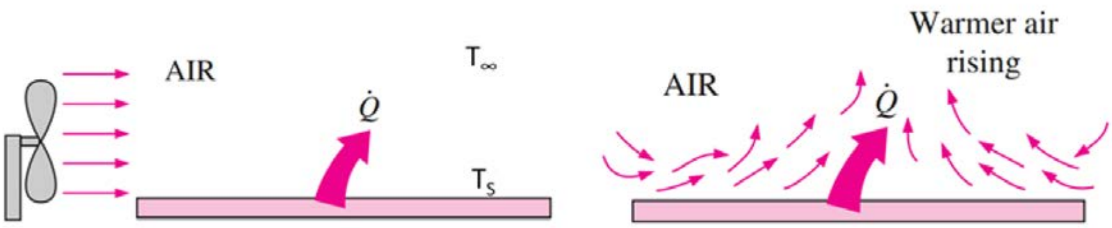

Figure 23. Forced and natural convection.

The heat flow depends on the properties of the fluid in motion and the shape and the nature of the surface from which the heat is transferred. Newton's law of cooling states that the rate of convection heat transfer is proportional to the temperature difference between the surface and the fluid:

$$\dot{Q} = hA(T_s - T_\infty), \tag{8}$$

where h is the heat transfer coefficient, T_s is the surface temperature and T_∞ is the fluid temperature. (Holman 2010; Kotandaraman 1998.)

3.2.3 Radiation

Thermal radiation is electromagnetic radiation by a body at the expense of its internal energy, the energy being transferred by photons. While the transfer of energy by conduction requires the presence of a material medium, radiation does not and in fact it occurs most efficiently in vacuum. Thermal radiation is of the same nature than other electromagnetic radiations like x rays and radio waves but has a different wavelength, from 0.1 to 100 µm. Thermal radiation between a surface with an area A_s at temperature T_s and a much larger surface at temperature T_{surr} is presented in Figure 24.

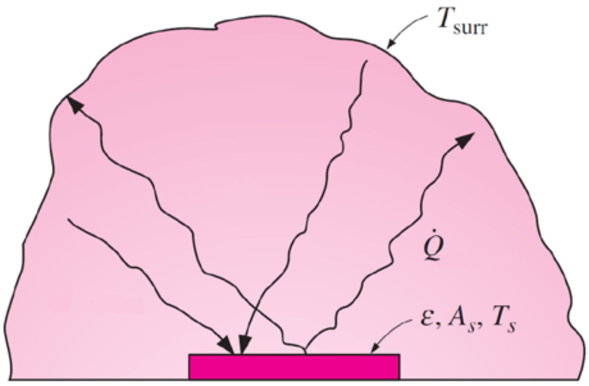

Figure 24. Radiation heat transfer between a surface enclosed by a bigger surface.

The rate of radiation heat transfer between the surfaces is

$$\dot{Q} = \varepsilon\sigma A_s(T_s^4 - T_{surr}^4), \tag{9}$$

where ε is emissivity and σ is Stefan-Boltzmann constant. Radiation is usually negligible in forced convection applications, especially when the surfaces have low to moderate temperatures. (Cengel 2002.)

3.3 Forced convection

Although the theory of fluid flow is well understood, theoretical solutions are obtained only for a few simple cases. Therefore, experimental results and empirical relations are used to analyse heat transfer in most cases. The experimental data for forced convection heat transfer is often represented with reasonable accuracy by a power-law relation

$$Nu = C Re^m Pr^n, \tag{10}$$

where *Nu* is Nusselt number, *Re* is Reynold's number and *Pr* is Prandtl number. *C*, *m* and *n* are empirical constants.

The type of the flow regime can be described by using **Reynold's number**, a ratio of the inertia forces, which are proportional to the density and the velocity of the fluid, to the viscous forces in the fluid. At large Reynolds numbers the inertia forces are large relative to the viscous forces causing random and rapid fluctuations of the fluid, leading to a turbulent flow. At small Reynolds numbers, the viscous forces are large enough to overcome the inertia forces to keep the fluid steadier, leading to a laminar flow. Reynold's number is defined as

$$Re = \frac{\rho u L_c}{\mu}, \tag{11}$$

where u is the flow speed, L_c is the characteristic length of the flow and μ is the dynamic viscosity of the fluid. (Cengel 2002.)

Prandtl number, the ratio of kinematic viscosity to thermal diffusivity, is given by

$$Pr = \frac{\mu c_p}{k}. \tag{12}$$

Finally, the Nusselt number and heat transfer coefficient have the relationship

$$Nu = \frac{hL_c}{k}. \tag{13}$$

The procedure above can be used to define a theoretical value for heat transfer coefficient.

3.3.1 Internal flow in a circular tube

Internal flow refers to a fluid transport in a circular or noncircular tube. To be practical, the fluid flow can be approximated to be one-dimensional. Thus the properties can be assumed to be uniform at any cross section and vary only in the direction of the flow. Because of no-slip condition, the fluid velocity in a tube changes from zero at the surface to a maximum u_{max} at the tube center. Therefore it is convenient to use an average value for the velocity u_{m}, which is derived from the conservation of mass principle requirement. Also the temperature T changes from T_s at the surface of the wall to maximum or minimum at the tube center. Thus it is convenient to use the mean temperature value T_m, which is derived from the conservation of energy principle requirement. The actual and idealized distributions for the fluid velocity and temperature are shown in Figure 25. (Cengel 2002.)

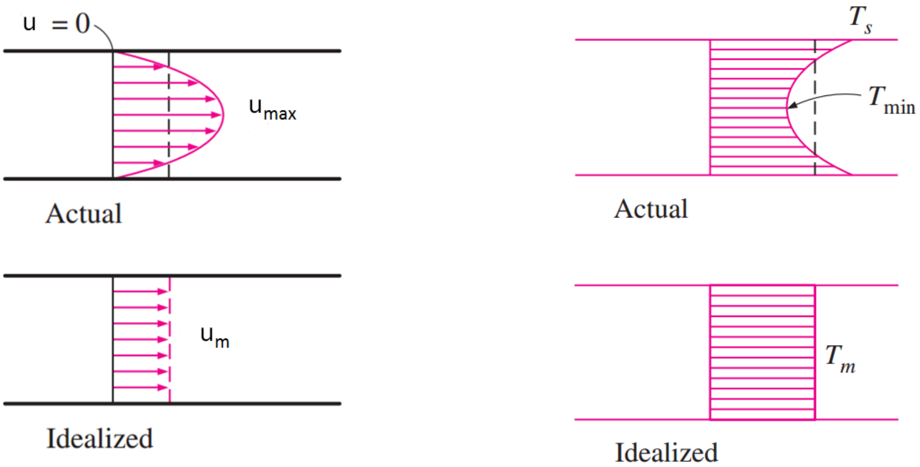

Figure 25. The actual and idealized flow speed and temperature distributions.

The fluid flow can be divided into three regions in the direction of the flow: laminar, transitional and turbulent. Transition from laminar to turbulent flow does not happen suddenly but in between them is a transitional region where the flow fluctuates between laminar and turbulent before becoming fully turbulent. Under most practical conditions, the flow in a tube is laminar for *Re* < 2300, turbulent for *Re* > 10000 and transitional in between. (Cengel 2002.)

For smooth tubes (no friction), Nusselt number for laminar flow is given by

$$Nu = 3.66 \tag{14}$$

and for fully turbulent flow by

$$Nu = 0.023 Re_D^{0.8} Pr^n, \tag{15}$$

where n = 0.4 is for heating and n = 0.3 is for cooling.

3.3.2 External flow over a flat surface

This chapter presents a flow case where a fluid flows parallel over a flat surface, having length L and surface temperature T_s (Figure 26). The fluid, with speed u_∞ and temperature T_∞, is laminar until point x_c, where a critical Reynold's number Re_{xc} (~ 5×10^5) is achieved. After this point the flow is turbulent.

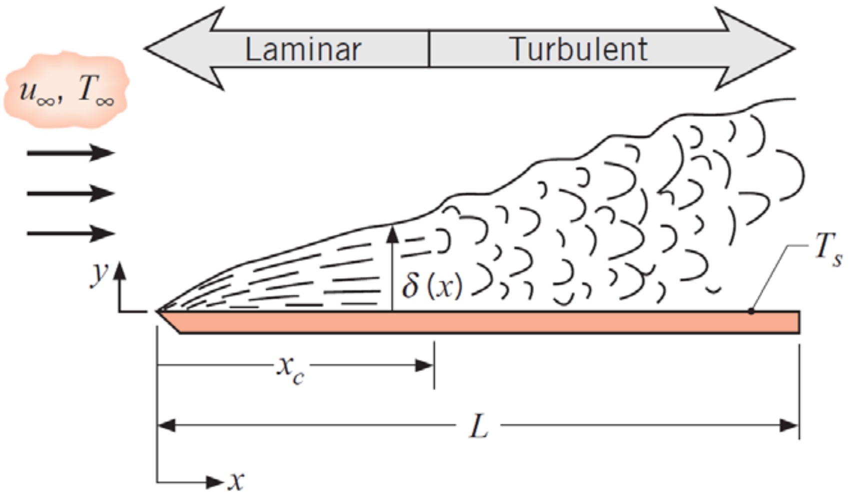

Figure 26. Parallel flow over a flat surface.

Nusselt number for laminar domain is defined as

$$Nu = 0.664\, Re_L^{0.5}\, Pr^{1/3} \tag{16}$$

and for turbulent domain as

$$Nu = 0.037\, Re_L^{0.8}\, Pr^{1/3}. \tag{17}$$

4 THERMO-MECHANICAL MODEL DESCRIPTION

This chapter presents the thermo-mechanical finite element modelling in detail.

4.1 Geometry

The geometry was created in CATIA and then implemented in ANSYS Workbench, the different components being simplified in the process. The module consists of two girders (MB and DB) supporting the RF structures by means of V-shaped supports. A 3D view of the geometry is shown in Figure 27. The materials used in the model are oxygen free copper (RF structures), silicon carbide (supports) and stainless steel (vacuum components).

Solid, shell and line elements have been used in the model. Solid elements have been used for components like girders and RF structures whereas shell elements have been used to model the thin-walled parts like VR. Line elements have been used to model the cooling channels. The model contains 1302154 elements and 2608063 nodes. The meshing strategy is shown in Figure 28.

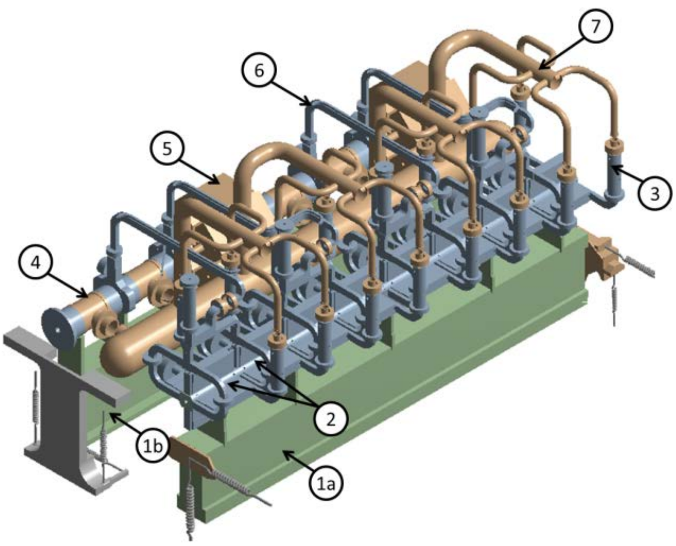

1a	Main Beam girder
1b	Drive Beam girder
2	SAS
3	Compact Load
4	PETS Unit
5	DBQ
6	RF network
7	Vacuum network

Figure 27. 3D view of the geometry.

Figure 28. Left: VR (shell). Middle: SAS (solid). Right: SAS+CL cooling channel (line).

4.1.1 Modelling of cavities

The MB and DB cavities have been modelled using cylindrical solid bodies with no stiffness or density; the solids are in contact with the internal surfaces of the drift tubes (Figure 29). The alignment of the beam axis is calculated in 9 reference points for MB (Figure 30) and in 8 for DB (Figure 31).

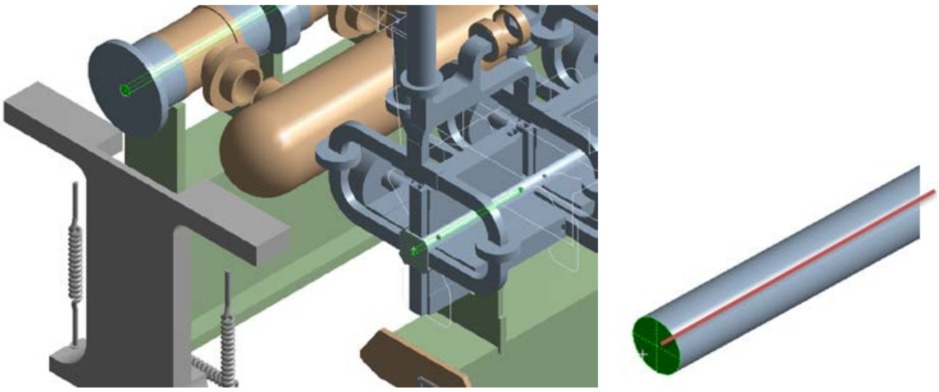

Figure 29. Cylindrical solids representing the cavities.

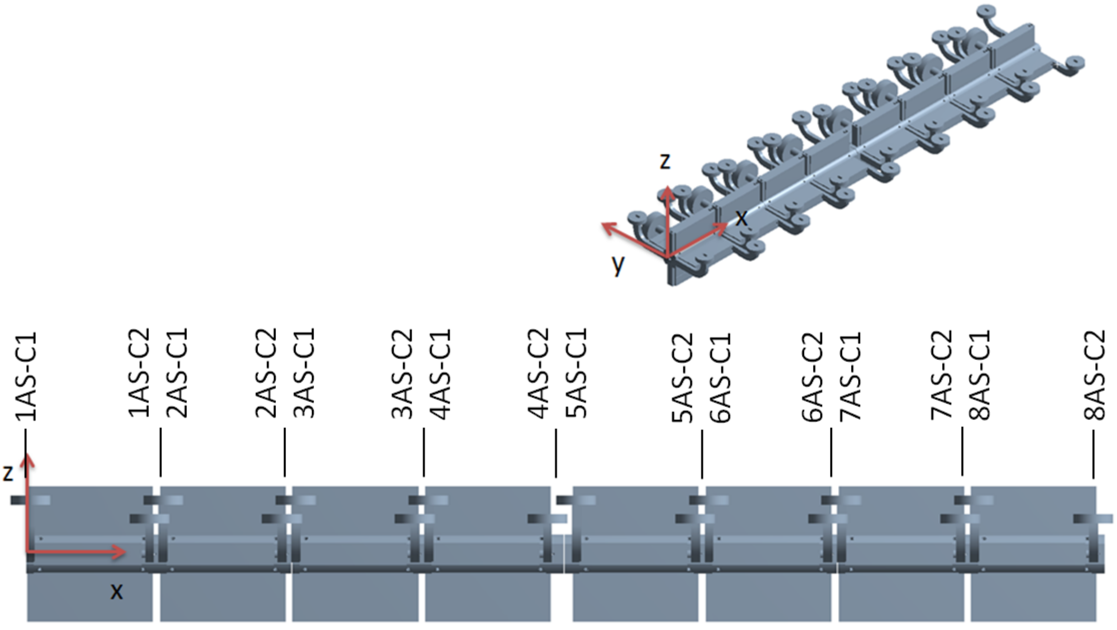

Figure 30. Reference points for MB axis.

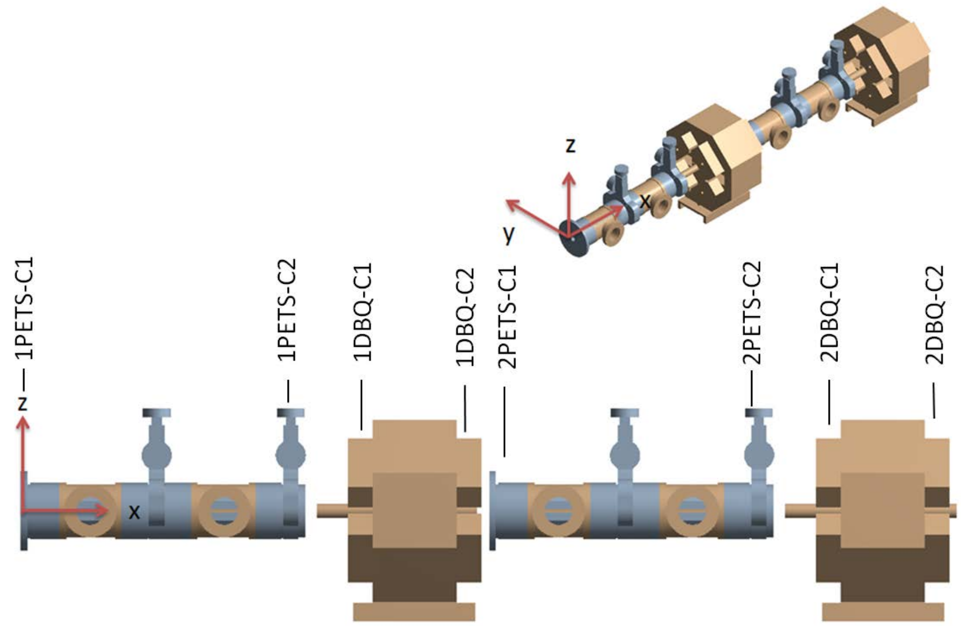

Figure 31. Reference points for DB axis.

4.2 Boundary conditions and constraints

The boundary conditions of the module are shown in Figure 32. The girders are supported by linear actuators which are modelled using equivalent stiffness elements. The longitudinal movement of both of the girders is fixed in one extremity while allowed in the other. The girders support the RF structures by means of V-shaped supports. SAS mock-up and PETS units are rigidly fixed to the middle supports. The sliding over the other supports in longitudinal direction is allowed in order to cope with the axial deformations due to thermal expansion.

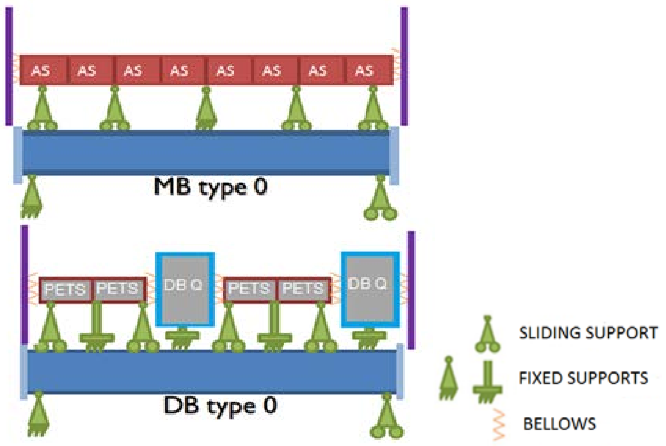

Figure 32. Boundary conditions of CLIC prototype module type 0.

4.2.1 Actuators

Cradles for MB and DB have been modelled at the extremities of the girders. The master cradles contain three (two vertical and one radial) actuators while the slave cradles are equipped with one vertical and one radial actuator, which have been modelled using equivalent stiffness elements. The cradles and corresponding actuators for MB and DB are shown in Figure 33.

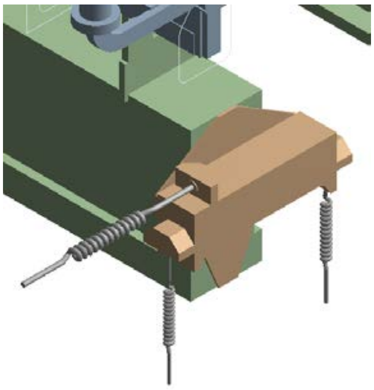

(A)

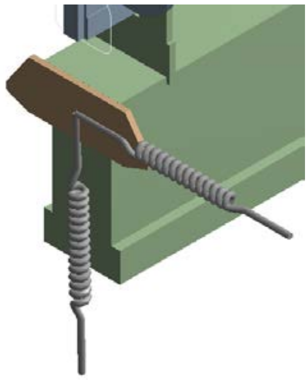

(B)

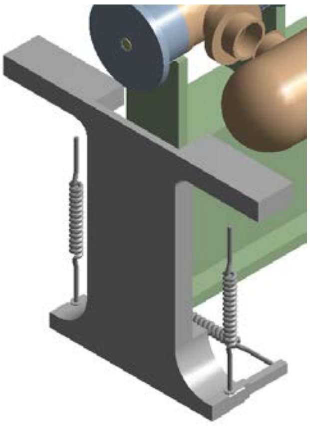

(C)

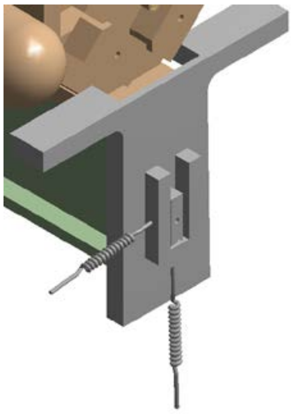

(D)

Figure 33. MB master cradle (A), MB slave cradle (B), DB master cradle (C) and DB slave cradle (D) as modelled in ANSYS.

4.2.2 Bellows

The behaviour of the bellows has been modelled using equivalent stiffness elements with four degrees of freedom: axial, angular, lateral and torsional (Figure 34). The values for the equivalent stiffness matrix have been taken from catalogues of leading firms for similar geometries (BOA, Witzenmann); Table 4 presents the stiffness values for VR bellows (PETS and SAS). The modelling of the bellows for PETS, SAS, RFN and CL are shown in Figure 35, while the real bellows are shown in Figure 18.

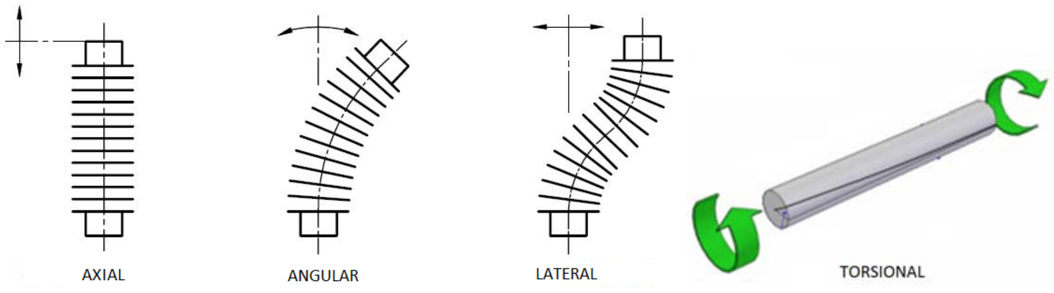

Figure 34. Degrees of freedom of the bellows.

Table 4. Stiffness values for SAS and PETS bellows.

Degree of freedom	**Value**
Axial (N/mm)	17.9
Angular (Nm/deg)	0.20
Lateral (N/mm)	5000
Torsional (Nm/deg)	100

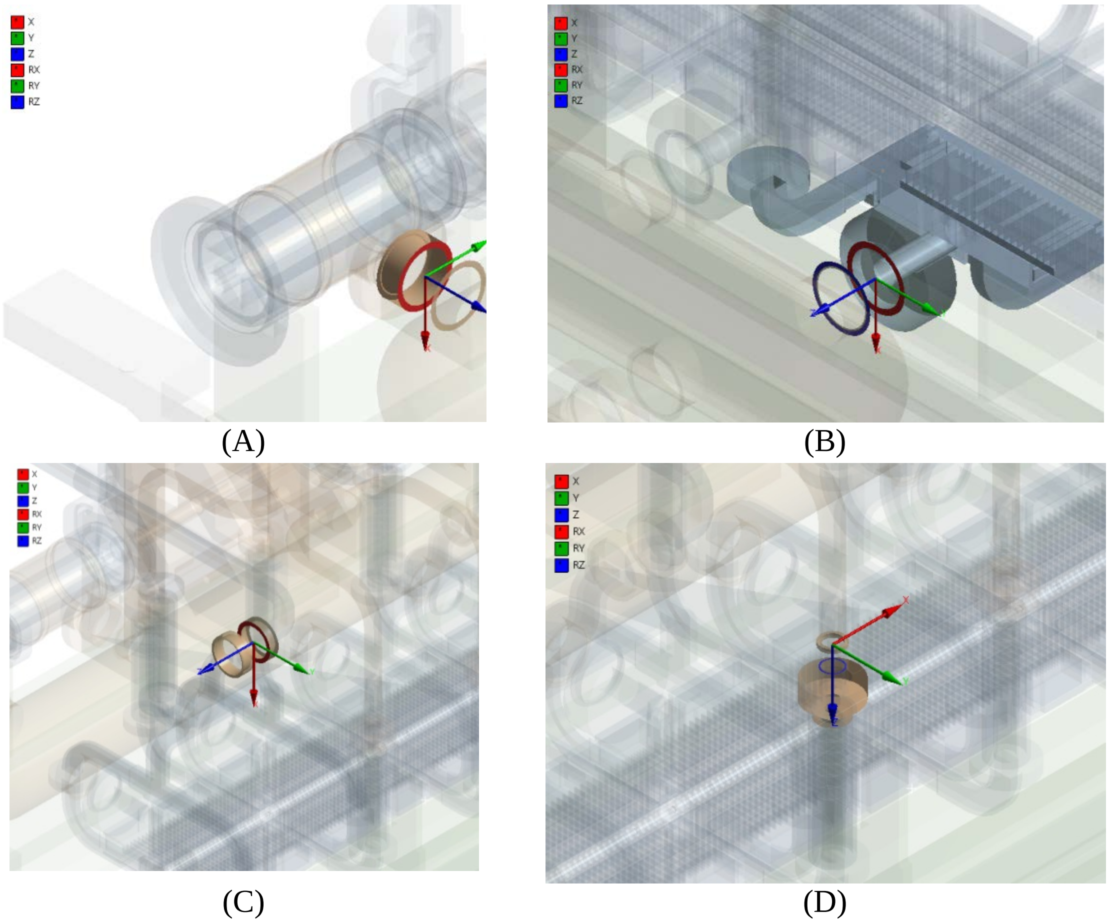

Figure 35. Bellows modelling for PETS (A), SAS (B), RF network (C) and CL (D).

4.3 Cooling system

The module cooling system consists of water cooling channels, modelled using line elements. A fraction of the heat is also transferred to air from the outer surfaces of the module via convection.

4.3.1 Cooling channels

The water cooling system includes five cooling circuits. Four of the circuits are located in the MB side of the module, cooling each one of the SAS and the corresponding CL (Figure 36), while one circuit is cooling the PETS units, WG and RFNL (Figure 37). The properties of the cooling channels are presented in Table 5. A script which allows the automatic calculation of the heat transfer coefficient h_w based on the mass flow and material properties of water has been developed in ANSYS; the calculations have been done according to the theory presented in chapter 3 for internal flow in circular tube.

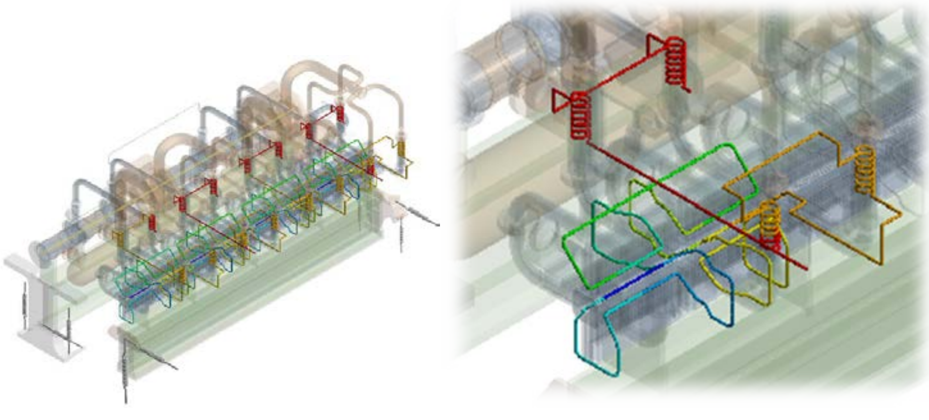

Figure 36. Left: 4 SAS+CL cooling channels. Right: Detailed view of the 1st SAS+CL cooling channel.

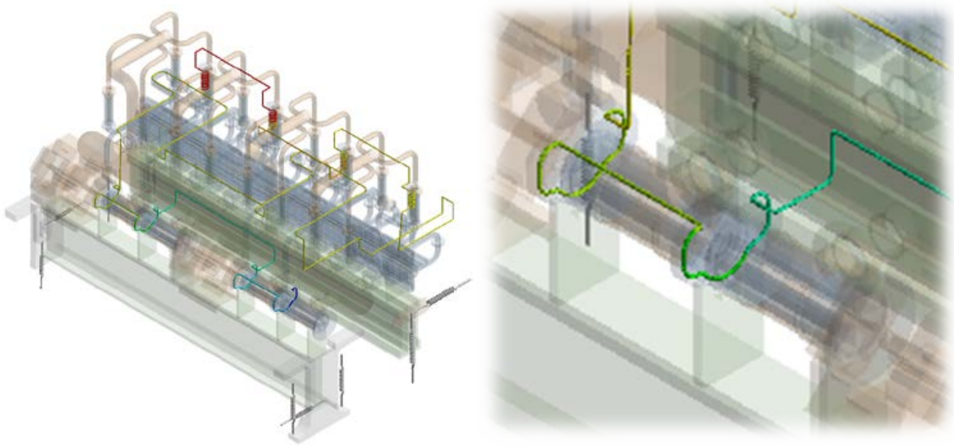

Figure 37. Left: PETS+WG+RFNL cooling channel. Right: Detailed view of the PETS+WG+RFNL cooling channel inside PETS unit.

Table 5. Properties of the cooling channels (CLIC baseline values).

Property	SAS+CL	PETS+WG+RFNL
Inlet temperature T_i (°C)	25	25
Mass flow $\dot{V}$ (m^3/h)	0.0686	0.0374
Heat transfer coefficient h_w (W/m^2·°C)	3935	2527

4.3.2 Heat dissipation to air

Heat dissipation to air from the outer surfaces of the module has been taken into account in the model by imposing a convection boundary condition on the outer surfaces of the module (Figure 38). The heat transfer coefficient to air h_a has been calculated based on the speed and material properties of air, according to theory presented in chapter 3 (laminar flow over flat surface). The properties of the air cooling are presented in Table 6.

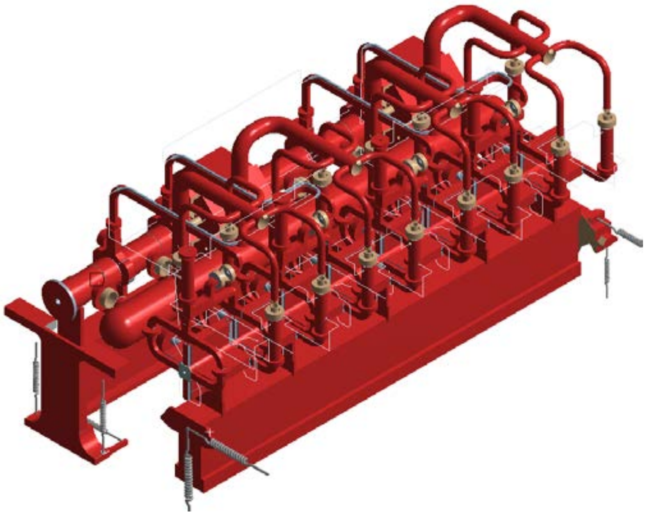

Figure 38. Convection to air surfaces.

Table 6. Air properties (CLIC baseline values).

Property	**Value**
Air speed u_∞ (m/s)	0.7
Ambient temperature T_∞ (°C)	40
Heat transfer coefficient h_a (W/m^2·°C)	4

4.4 Load Conditions

4.4.1 Heat loads

Thermal loads are considered in the simulation to calculate both the temperature distribution of the module and the resulting misalignments of the beam axes. Nominal heat powers for different components according to Stapnes et al. (2012) are presented in Figure 39 and Table 7.

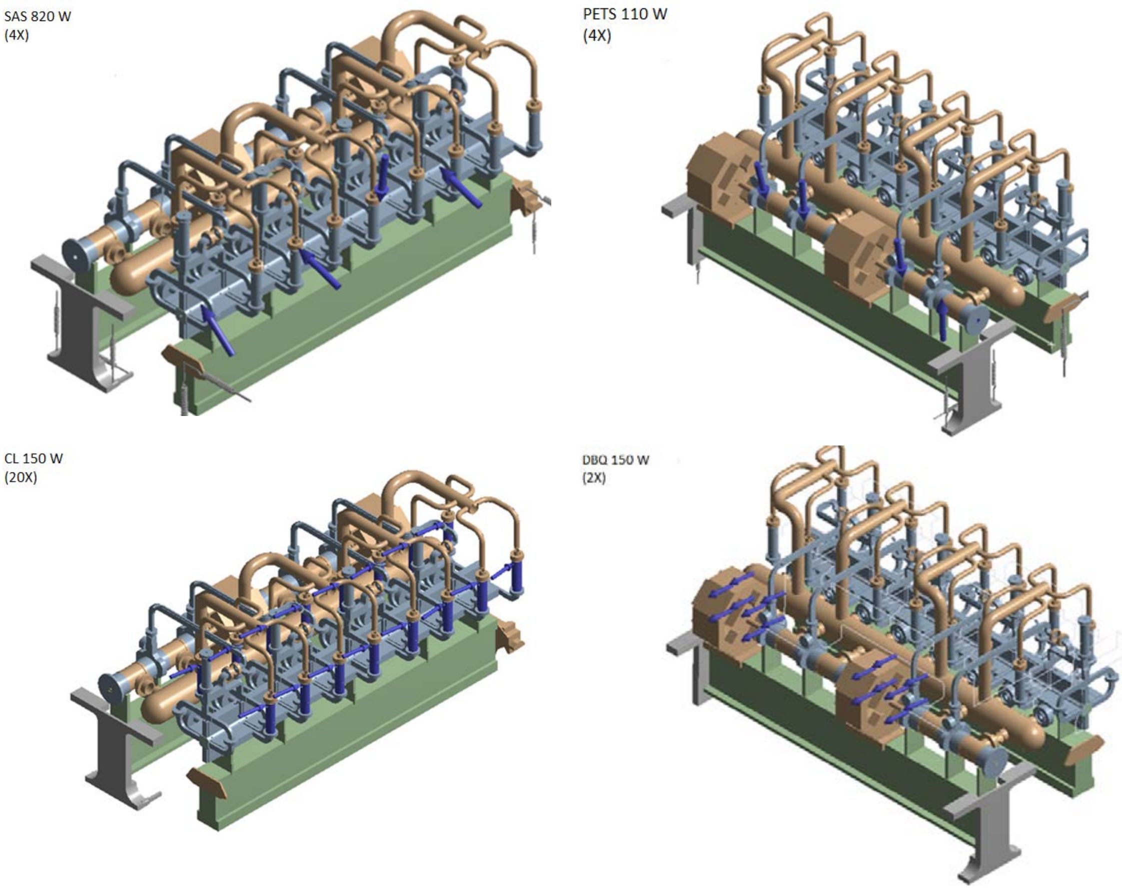

Figure 39. Heat load definitions for SAS, PETS, CL and DBQ.

Table 7. Nominal heat powers.

Item	Heat power (W)
SAS	820
PETS	110
CL	150
DBQ	150

4.4.2 Gravity

The earth's gravity has been taken into account by imposing an acceleration of 9.81 m/s^2 in z direction, shown in Figure 40.

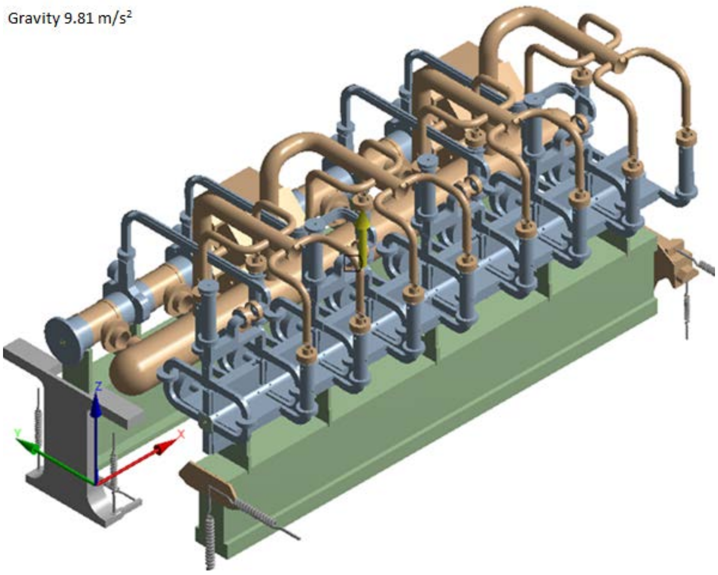

Figure 40. Gravity load.

4.4.3 Vacuum

The vacuum condition has been taken into account by imposing an external pressure of 1 bar on the outer surfaces of the structure. Vacuum load is shown in Figure 41.

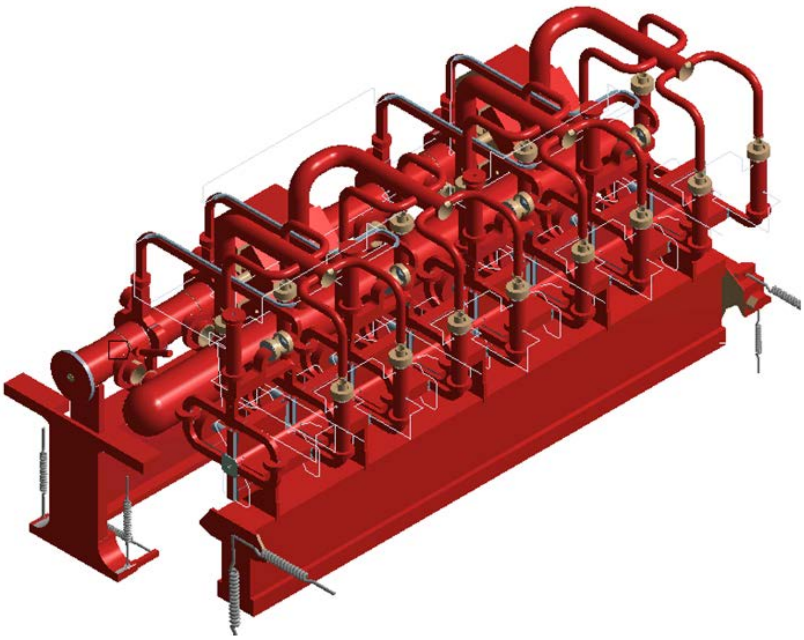

Figure 41. Vacuum load.

5 EXPERIMENTAL TEST PROGRAM

This chapter presents the thermal test program defined for CLIC prototype module type 0 assembled in a dedicated laboratory (Figure 42). The aim of the tests is to study the thermo-mechanical behaviour of the module under different operating conditions.

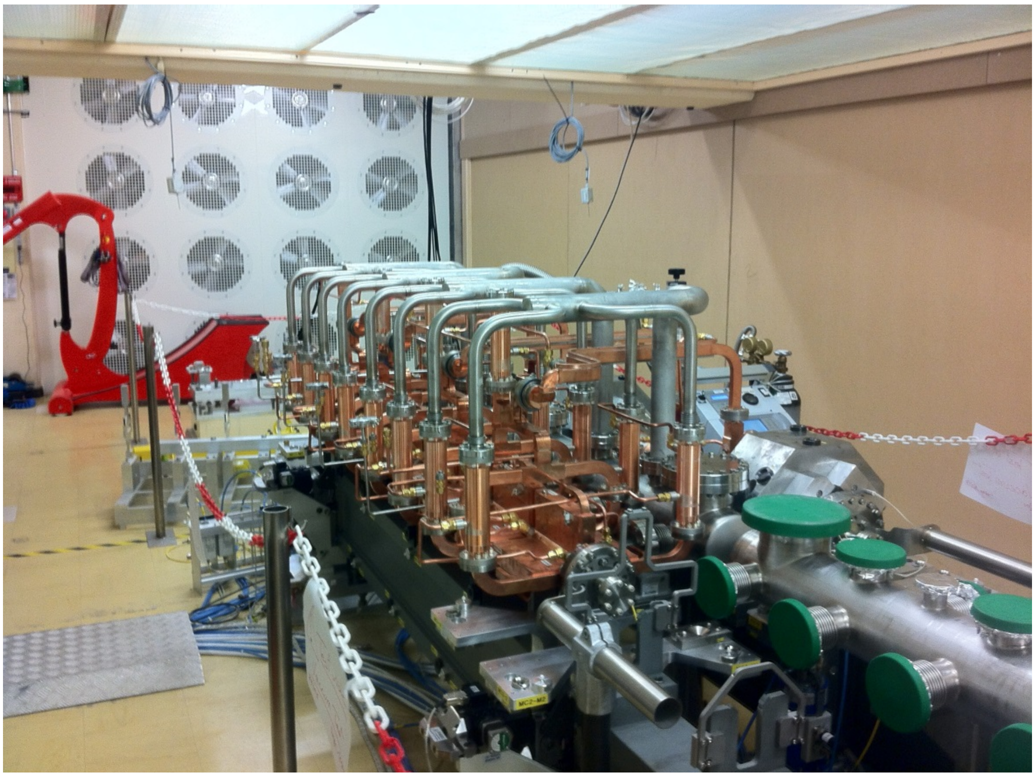

Figure 42. The CLIC prototype module 0 inside the dedicated laboratory.

5.1 Heating system

The power dissipation in the RF structures (Table 1) is reproduced by using electric heaters (Figure 43). AS and PETS units are heated with straight tubular heaters while cartridge heaters are used for DBQs and silicon rubber heaters for CLs. The power of the heaters is regulated by two different controllers: Solid State Relays (SSR) is used for AS, PETS and DBQs and Semi-Conductors Relays (SCR) for CL. The aim is to test and compare the different systems.

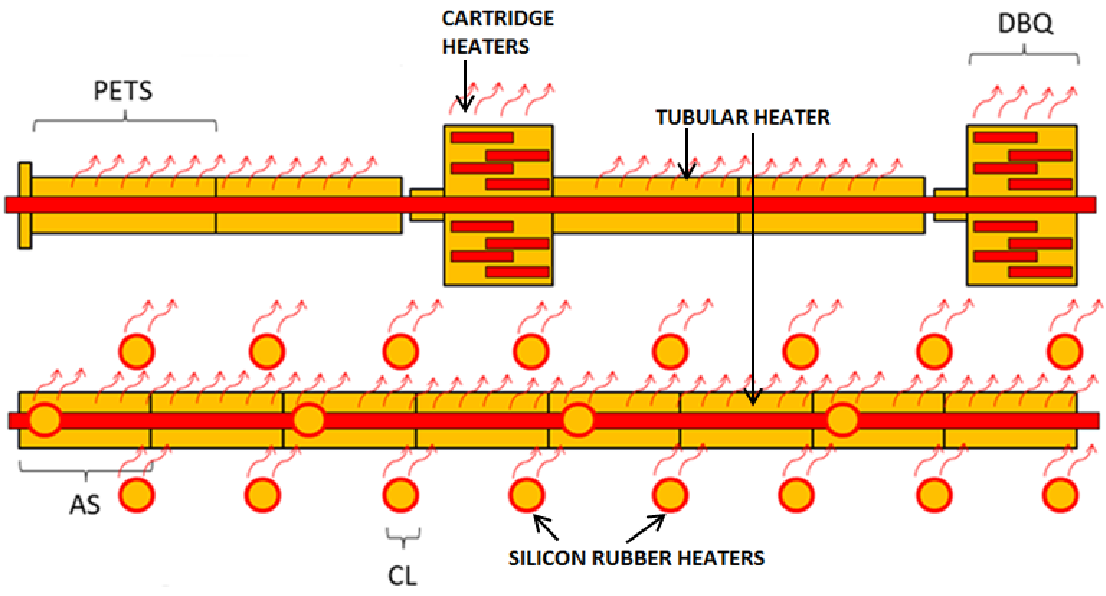

Figure 43. Heaters inside RF structures.

5.2 Water cooling system

A water cooling system has been integrated in the module to remove the heat generated in different components (Figure 13). The flow rate is regulated using solenoid control valves (CV). By adjusting the position of these valves via Proportional-Integral-Derivative (PID) controller, the outlet temperature of water can be controlled. An external water chiller is used to supply the water of needed temperature, while the inlet pressure is set by a pressure regulating valve (PRV).

5.3 Air conditioning and ventilation system

An air conditioning and ventilation system has been installed in the laboratory in order to reproduce similar air temperature and air flow conditions as in the CLIC tunnel (Figure 44). The air circulation is created using two sets of fans installed on the two sides of the laboratory; the first set blows the air towards the module while the second set sucks it from the opposite side. The air is recirculating through a lateral corridor where cooling and heating coils are installed for regulating the temperature. The temperature can be changed from 20 to 40 °C and the air speed from 0.4 to 0.8 m/s.

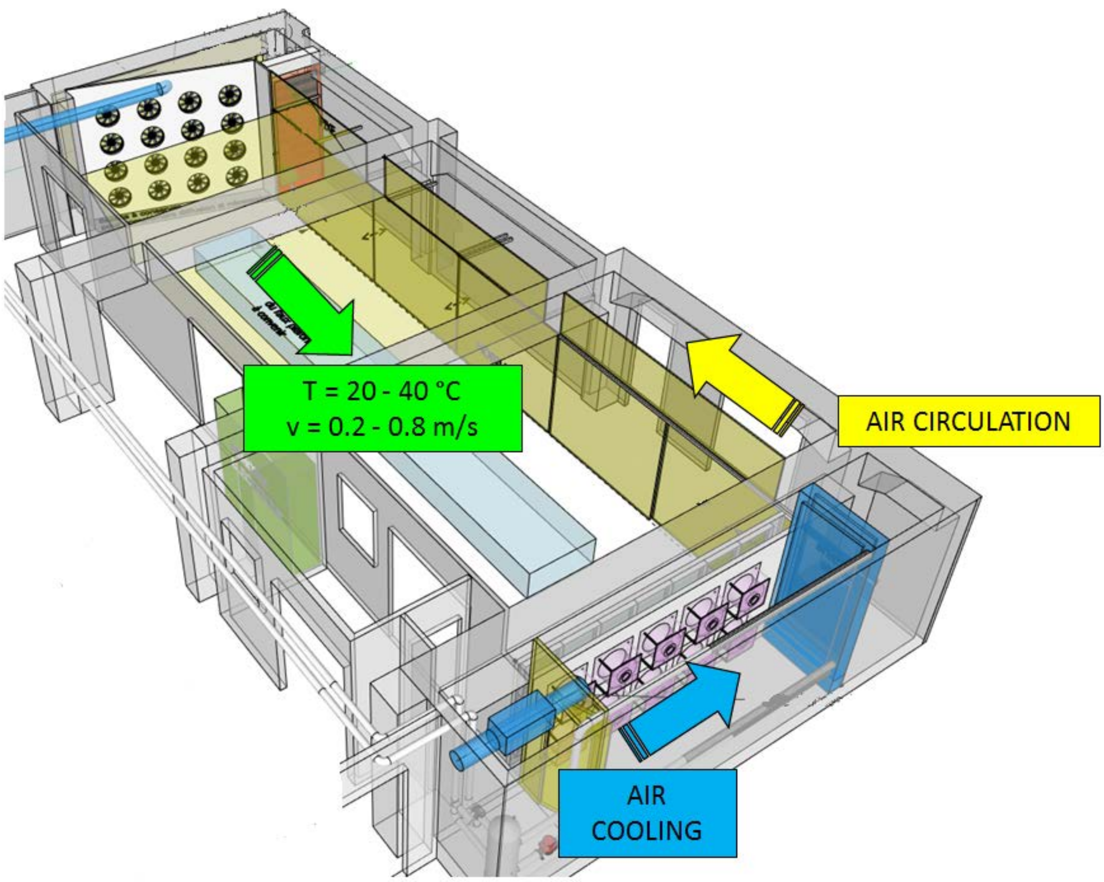

Figure 44. The air conditioning and ventilation system in the laboratory.

5.4 Data acquisition and control system

The temperature of the module is monitored and recorded throughout the tests with temperature sensors (Figure 45 and Figure 46), while the air temperature around the module is measured using thermocouples (Figure 47). Pressures and flow rates of the water cooling channels are also measured in real-time. Fiducials installed on the structure (Figure 48) and laser tracker devices are used to measure the alignment of the module, especially the alignment of the beam axes. (Rossi et al. 2013.)

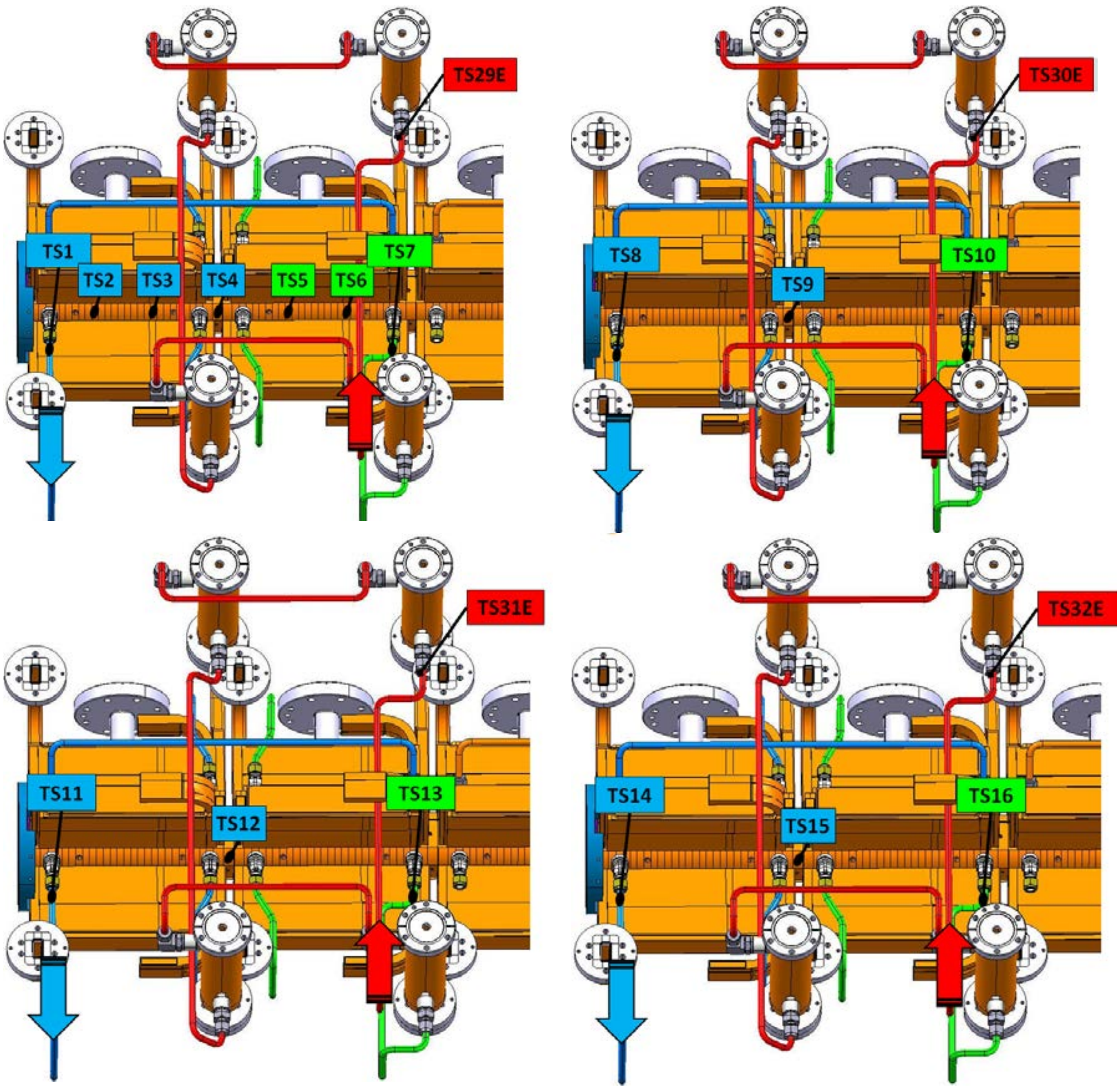

Figure 45. Temperature sensors on MB.

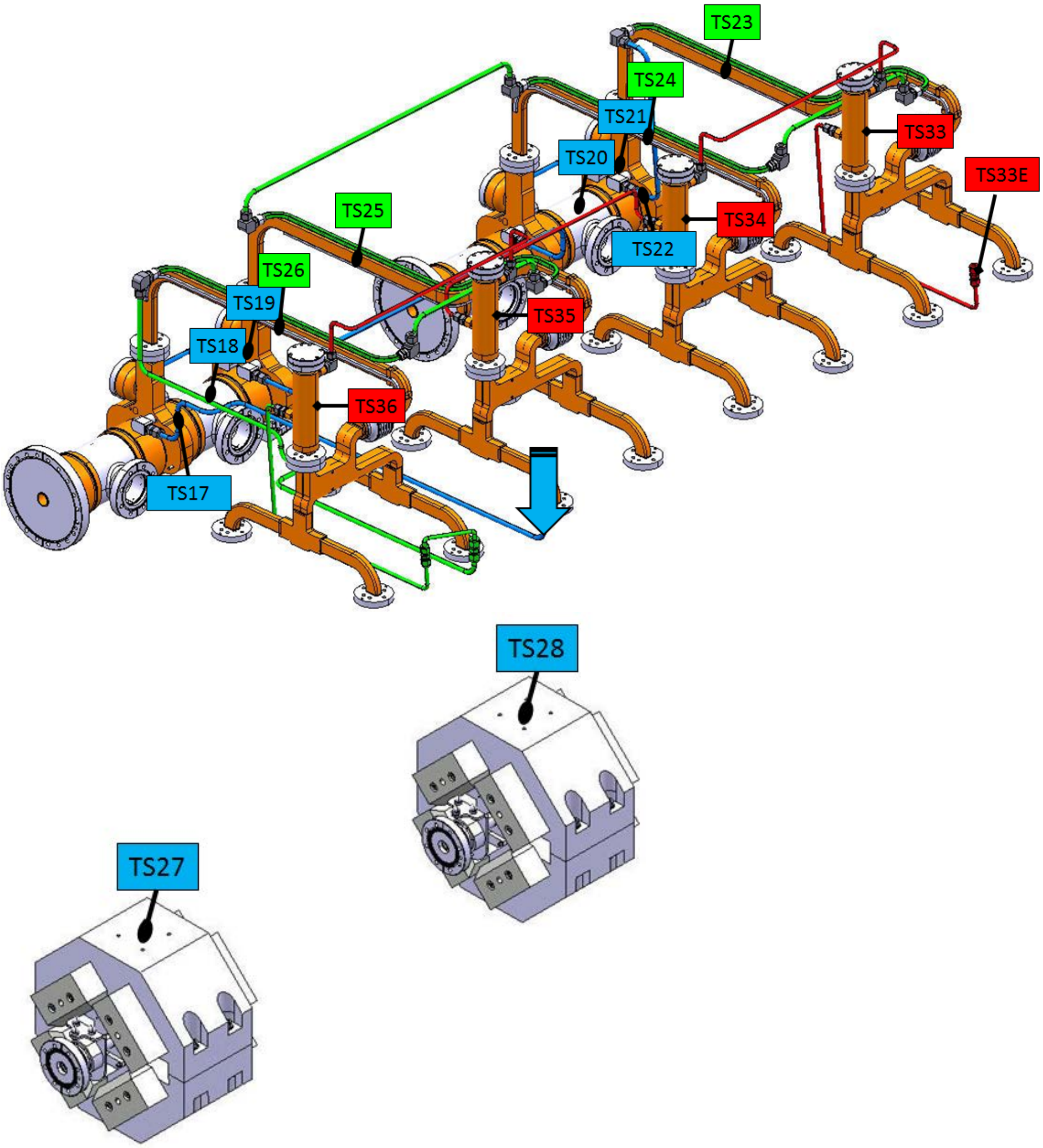

Figure 46. Temperature sensors on DB.

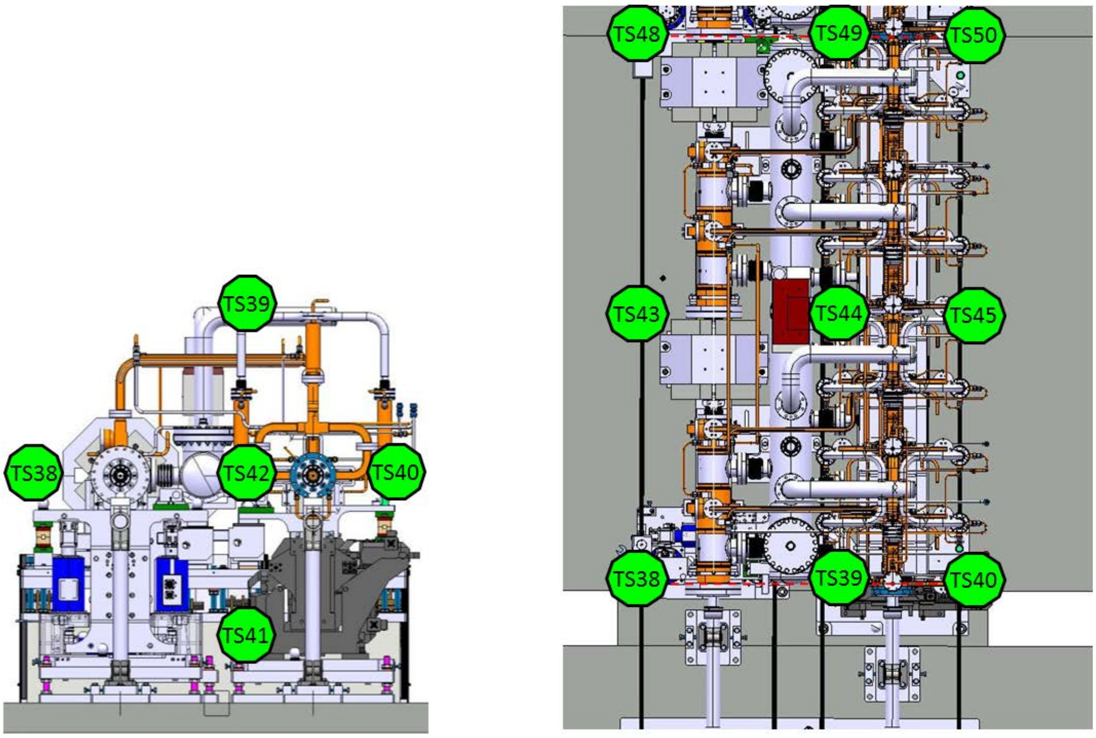

Figure 47. Thermocouples around the module.

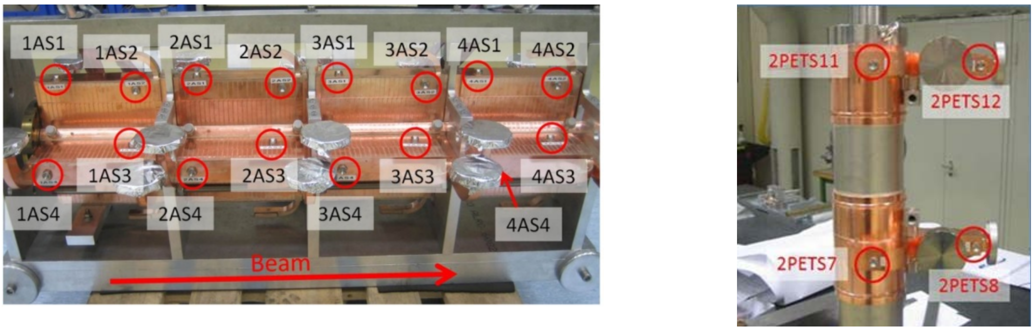

Figure 48. Fiducials on AS mock-up (left) and PETS unit (right).

5.5 Thermal test program

A short summary of the thermal test program is given below.

- STEP 0: the air speed is changed up to 0.8 m/s to study the influence of vibrations induced by the air circulation on the WPS measuring system.
- STEP 1: the room temperature is changed from 20 to 40 °C without any heating or cooling present in the module. The temperature and the alignment of the RF structures are measured.
- STEP 2: SAS and CL are heated gradually up to the maximum power while the water cooling system for these components is active. The temperature and the alignment of the RF structures are measured at different values of air temperature (20 and 40 °C) and speed (0.4 and 0.8 m/s).
- STEP 3: PETS, DBQ and RFN Loads are heated gradually up to the maximum power while the water cooling system for these components is active. The temperature and the alignment of the RF structures are measured at different values of air temperature (20 and 40 °C) and speed (0.4 and 0.8 m/s).
- STEP 4: All the components are heated gradually up to the maximum power while the water cooling systems are active. The temperature and the alignment of the RF structures are measured at different values of air temperature (20 and 40 °C) and speed (0.4 and 0.8 m/s).

6 RESULTS

The thermal test program consists of five different steps where, initially, the Main and Drive beam are tested separately and, finally, the thermo-mechanical behaviour of the module is studied by heating at the same time the accelerating structures, CL, PETS and DBQ. The overall strategy is summarized in Table 8.

In particular, in STEP 0 the influence of the vibrations induced by the air flow on the WPS measuring system is studied by changing the air speed from 0.3 to 0.8 m/s. During STEP 1 the alignment of the beams is measured at different room temperatures (20, 30 and 40 °C) while no heat power is generated for the MB and the DB. In STEP 2 and STEP 3, the alignment measurements are done while the MB and the DB are heated separately; firstly in STEP 2, only the SAS and the corresponding CL are tested at 50% and 100% of the nominal heat power, while the dissipated power is removed by the integrated water cooling system; temperature and alignment measurements are taken for different combinations of air temperature (20 and 40 °C) and air speed (0.4 and 0.8 m/s). Subsequently, in STEP 3, the same procedure is repeated by heating only the PETS, the CL of the hybrids and the DBQ. Finally, during STEP 4 all the components are heated at 50% and at 100% of the nominal power, while the water cooling systems are active. As done in the previous steps, the temperature and the alignment of the module are measured at different values of air temperature (20 and 40 °C) and speed (0.4 and 0.8 m/s).

The results of the alignment and temperature measurements are presented and the comparison with the numerical modelling is discussed in this chapter.

Table 8. Steps of the thermal test program.

STEP	#	INPUT											
		T_∞ (°C)	u_∞ (m/s)	$\dot{Q}$ (%)					$T_{i,water}$ (°C)	$T_{o,water}$ (°C)		$\dot{V}$ (m^3/h)	
				SAS	*AS Load*	*PETS*	*RFN Load*	*DBQ*		*SAS*	*PETS*	*SAS*	*PETS*
0	0.1	20	0.3	0	0	0	0	0	-	-	-	-	-
	0.2	20	0.4	0	0	0	0	0	-	-	-	-	-
	0.3	20	0.5	0	0	0	0	0	-	-	-	-	-
	0.4	20	0.6	0	0	0	0	0	-	-	-	-	-
	0.5	20	0.7	0	0	0	0	0	-	-	-	-	-
	0.6	20	0.8	0	0	0	0	0	-	-	-	-	-
1	1.1	20	0.3	0	0	0	0	0	-	-	-	-	-
	1.2	30	0.3	0	0	0	0	0	-	-	-	-	-
	1.3	40	0.3	0	0	0	0	0	-	-	-	-	-
2	2.1	20	0.4	50	50	0	0	0	25	30	-	-	-
	2.2	20	0.4	100	100	0	0	0	25	35	-	-	-
	2.3	20	0.8	50	50	0	0	0	25	30	-	-	-
	2.4	20	0.8	100	100	0	0	0	25	35	-	-	-
	2.5	40	0.4	50	50	0	0	0	25	30	-	-	-
	2.6	40	0.4	100	100	0	0	0	25	35	-	-	-
	2.7	40	0.8	50	50	0	0	0	25	30	-	-	-
	2.8	40	0.8	100	100	0	0	0	25	35	-	-	-
3	3.1	20	0.4	0	0	50	50	50	25	-	-	-	0.0374
	3.2	20	0.4	0	0	100	100	100	25	-	-	-	0.0374
	3.3	20	0.8	0	0	50	50	50	25	-	-	-	0.0374
	3.4	20	0.8	0	0	100	100	100	25	-	-	-	0.0374
	3.5	40	0.4	0	0	50	50	50	25	-	-	-	0.0374
	3.6	40	0.4	0	0	100	100	100	25	-	-	-	0.0374
	3.7	40	0.8	0	0	50	50	50	25	-	-	-	0.0374
	3.8	40	0.8	0	0	100	100	100	25	-	-	-	0.0374
4	4.1	20	0.4	50	50	50	50	50	25	-	-	0.0686	0.0374
	4.2	20	0.4	100	100	100	100	100	25	-	-	0.0686	0.0374
	4.3	20	0.8	50	50	50	50	50	25	-	-	0.0686	0.0374
	4.4	20	0.8	100	100	100	100	100	25	-	-	0.0686	0.0374
	4.5	40	0.4	50	50	50	50	50	25	-	-	0.0686	0.0374
	4.6	40	0.4	100	100	100	100	100	25	-	-	0.0686	0.0374
	4.7	40	0.8	50	50	50	50	50	25	-	-	0.0686	0.0374
	4.8	40	0.8	100	100	100	100	100	25	-	-	0.0686	0.0374

6.1 STEP 1

During STEP 1 the influence of the room temperature on the alignment of the beams is studied by changing the air temperature from 20 to 40 °C, while no heating and cooling are present inside the module. Alignment measurements, done by BE-ABP-SU, are performed at 20 °C (STEP 1.1), 30 °C (STEP 1.2) and 40 °C (STEP 1.3). By measuring the position of the fiducials on the RF structures with the laser tracker Leica AT401

(Griffet et al. 2012), the alignment of the beam axes is then derived. At the same time the temperature of the RF structures is monitored and recorded throughout the tests by means of the sensors attached to them. Figure 49 shows the measured and predicted transient thermal response of the SAS by changing the room temperature from 20 to 30 °C; it is worth noting that the experimental transient time, almost twelve hours, is in agreement with the results of the numerical modelling.

The MB and DB displacements in the three spatial directions are shown in Figure 50 for an increase of temperature of ten degrees Celsius; the comparison between the predicted and the measured displacements of the beam axes are presented in Figure 51 and Figure 52. In each plot, the abscissa refers to the horizontal position along the MB and DB girders, while the ordinate represents the displacement in three directions x, y and z. The brown curve shows the absolute displacement of the MB and DB axis, while the red line represents the relative displacement of the beam axis with respect to the girder axis (yellow curve). The comparison of the red curve with the blue and azure ones, referring to the experimental measurements for an increase of temperature of 10 °C (from 20 to 30 °C and from 30 to 40 °C respectively), show that the numerical and experimental results are in agreement within a tolerance of ±10 μm, the same value as the overall accuracy of the experimental method used for the alignment measurements.

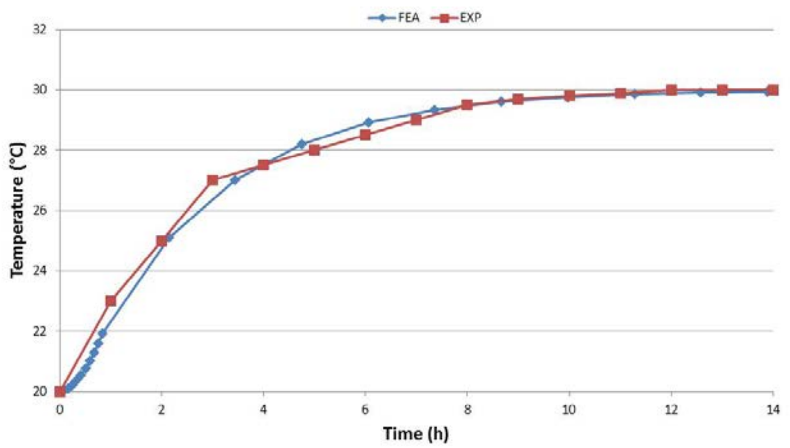

Figure 49. Transient thermal response of the SAS.

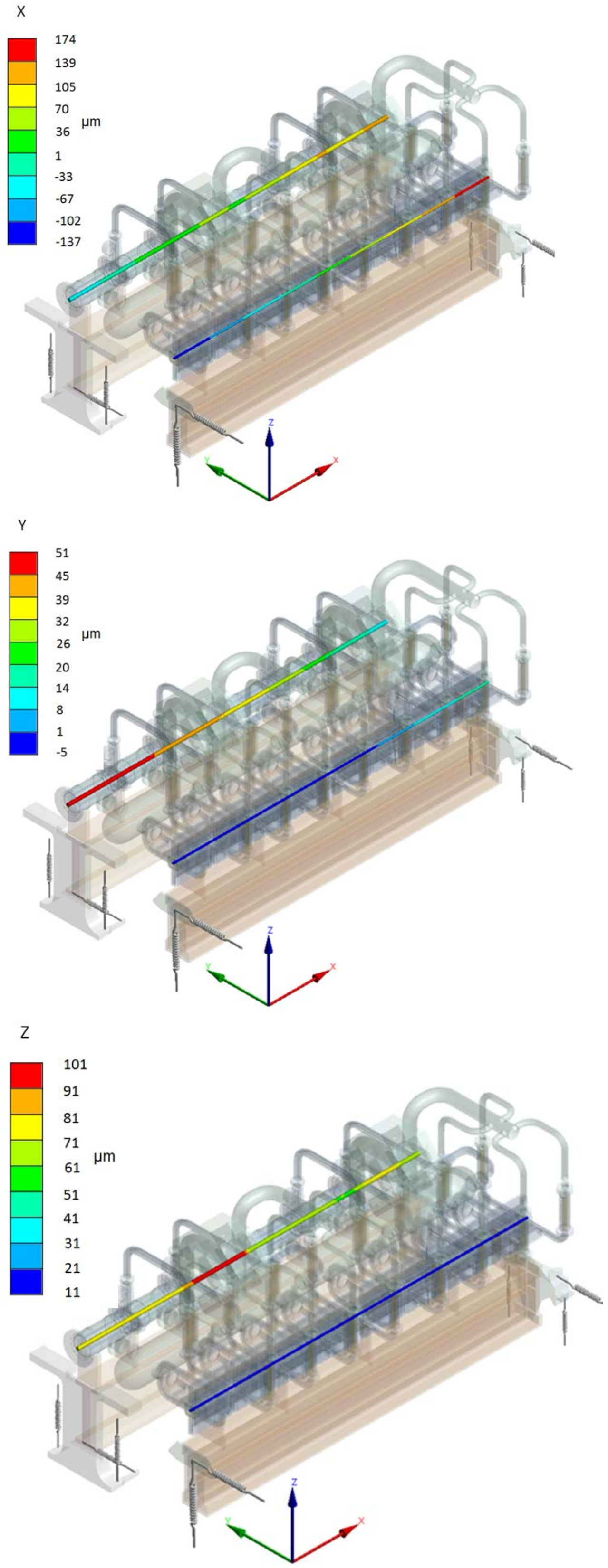

Figure 50. Resulting beam displacements in three directions (x,y,z) for an increase of temperature of 10 °C.

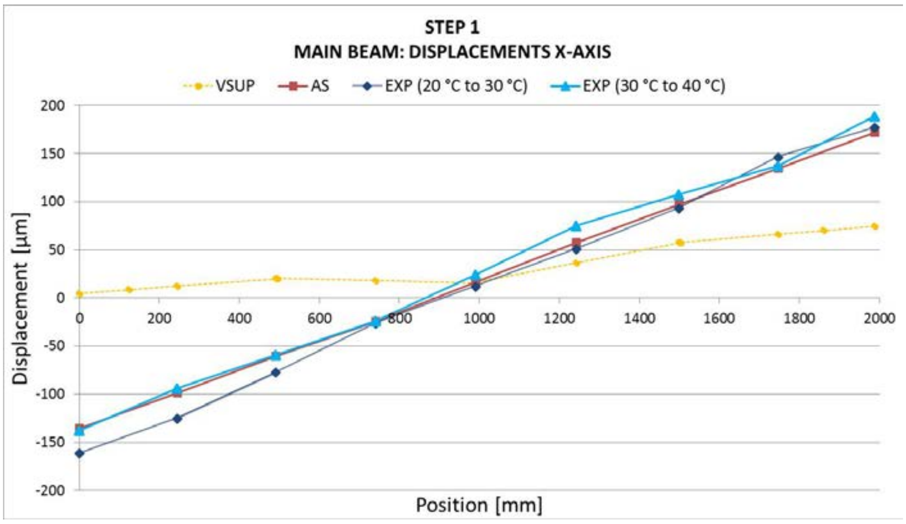

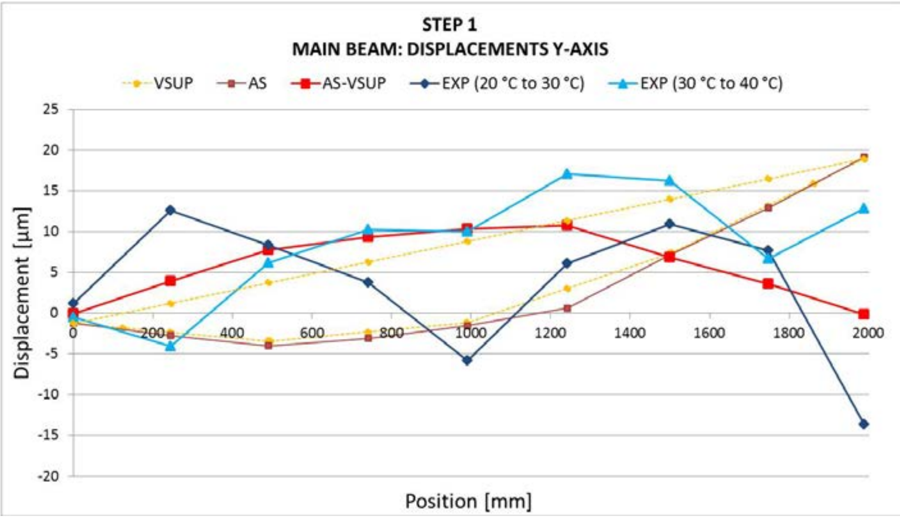

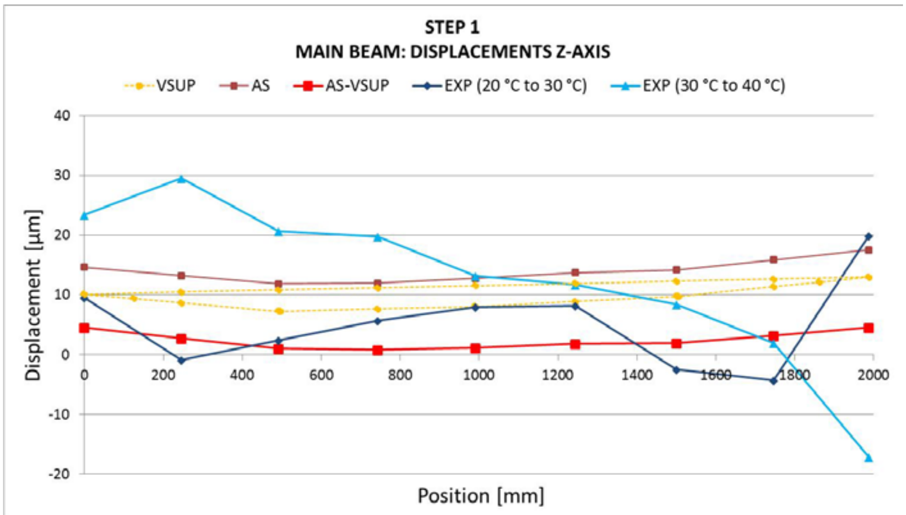

Figure 51. Displacements of MB in three directions for STEP 1.

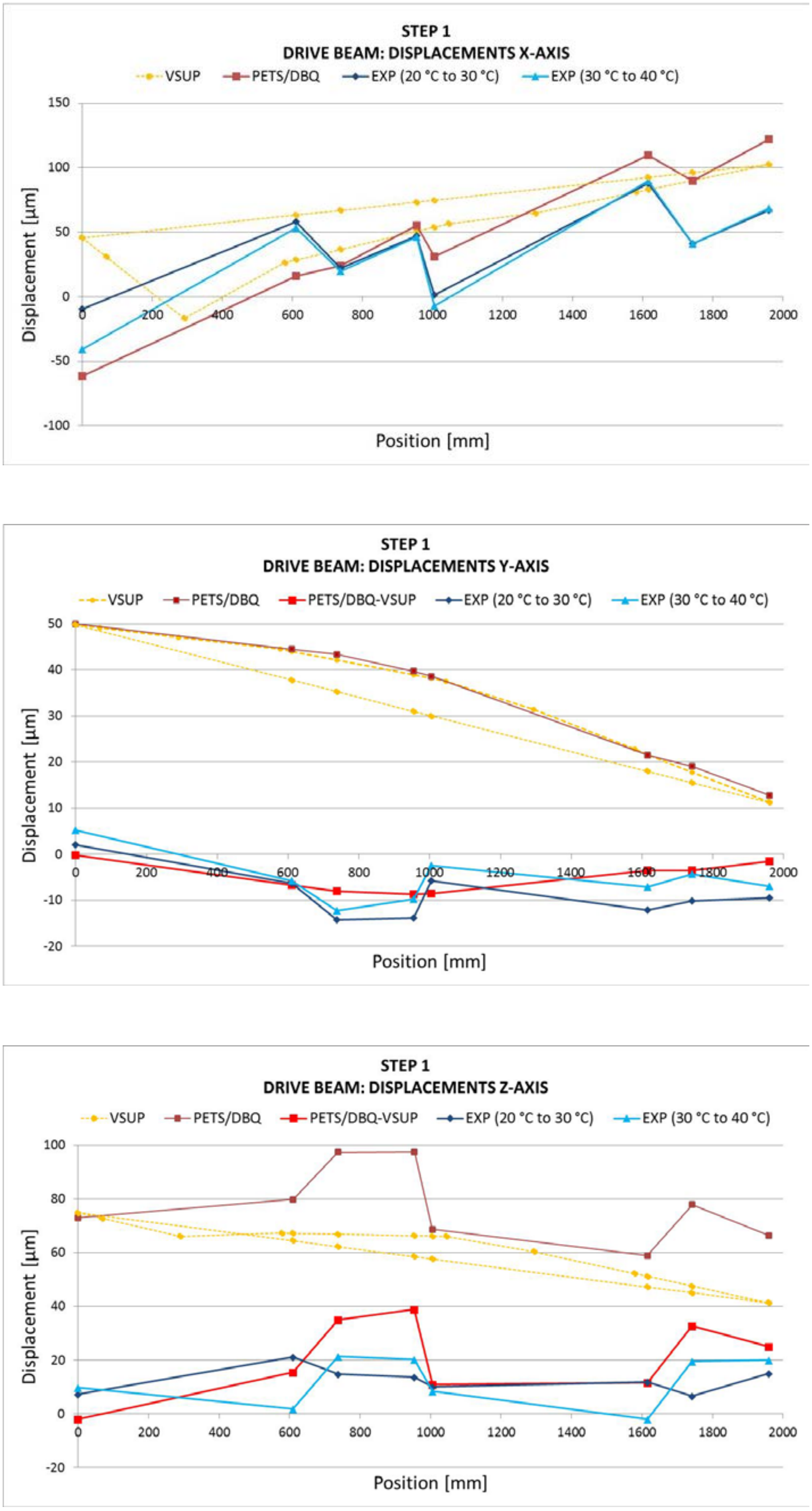

Figure 52. Displacements of DB in three directions for STEP 1.

6.2 STEP 2

In STEP 2 only the AS and the corresponding ASL are heated while the generated heat power is removed by the cooling channels, whereas PETS, DBQ and RFNL are not heated and cooled. The temperature measurements are done at different combinations of heat power percentage (50% and 100%), room temperature (20 and 40 °C) and air speed (0.4 and 0.8 m/s). The outlet temperature of the SAS cooling channel is imposed to have an increase of 5 °C for 50% of the total heat power. Since the surface temperature of the AS heater at 50% of the total heat power was exceeding the maximum temperature allowed by the manufacturer, the measurements at 100% have not been done. A new heater has been ordered and the measurements at 100% will be completed later.

The results of the temperature measurements for STEP 2.1 (room temperature 20 °C) and STEP 2.5 (room temperature 40 °C) are shown in Figure 53 and Figure 54 . The naming convention for the temperature sensors is the same as in Figure 45. The numerical values have been plotted for three different values of the heat transfer coefficient to air (h_a = 3.8, 16 and 38 W/m^2·°C). In STEP 2.1, the resulting surface temperature of the module is higher than the room temperature; the heat is flowing from the module to the air**.** By increasing the theoretical heat transfer coefficient, the surface temperatures calculated numerically are decreasing**.** In STEP 2.5 the behaviour is opposite; in this case, since the room temperature is higher than the surface temperatures of the module, increasing the heat transfer coefficient increases the surface temperatures. It can be seen that for STEP 2.1 the predicted temperatures for a heat transfer coefficient of ~38 W/m^2·°C (Figure 55) are in agreement with the experimental ones**,** while For STEP 2.5 the best correspondence is found for a heat transfer coefficient of 3.8 W/m^2·°C.

It is worth noting that the influence of the air speed on the resulting surface temperatures measured is almost negligible since the experimental curves for the two different air speeds are almost overlapping.

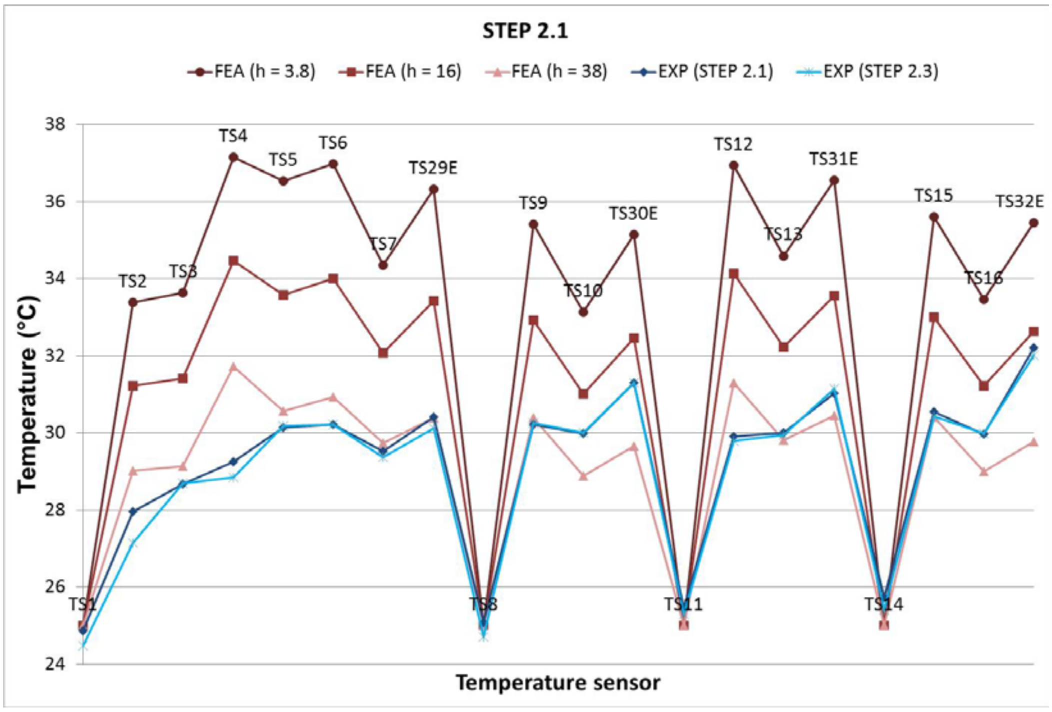

Figure 53. Temperature distribution of the module for STEP 2.1 ($\dot{Q}_{AS}$ = 50%, $\dot{Q}_{ASL}$ = 50%, $\dot{V}_{SAS}$ = 0.0345 m^3/h, T_∞ = 20 °C).

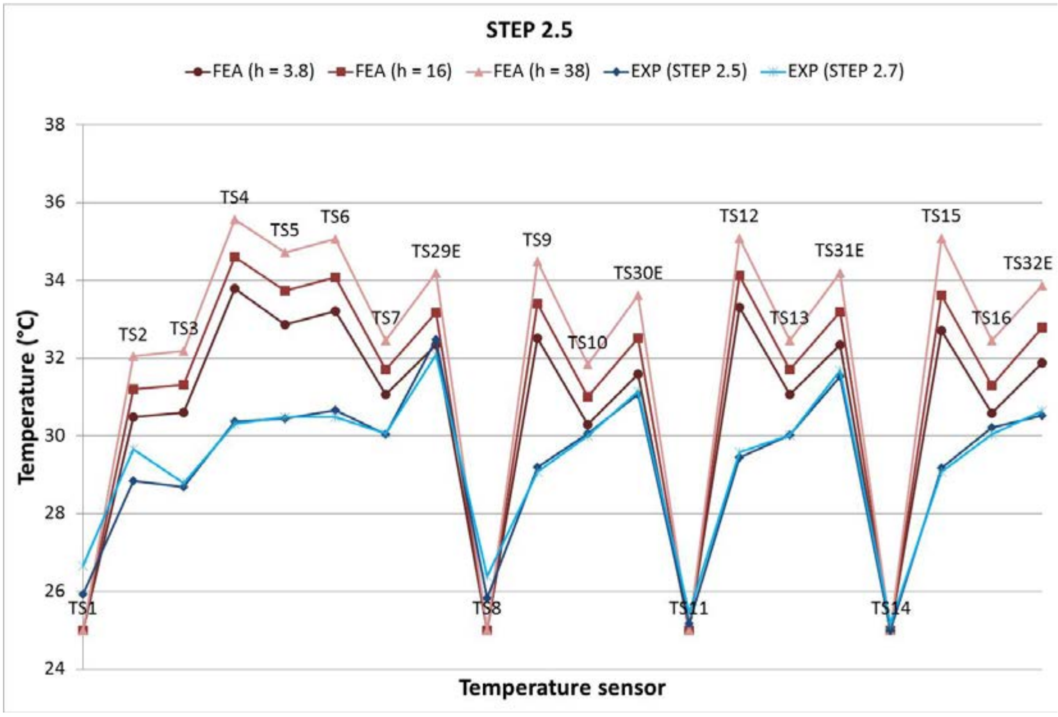

Figure 54. Temperature distribution of the module for STEP 2.5 ($\dot{Q}_{AS}$ = 50%, $\dot{Q}_{ASL}$ = 50%, $\dot{V}_{SAS}$ = 0.066 m^3/h, T_∞ = 40 °C).

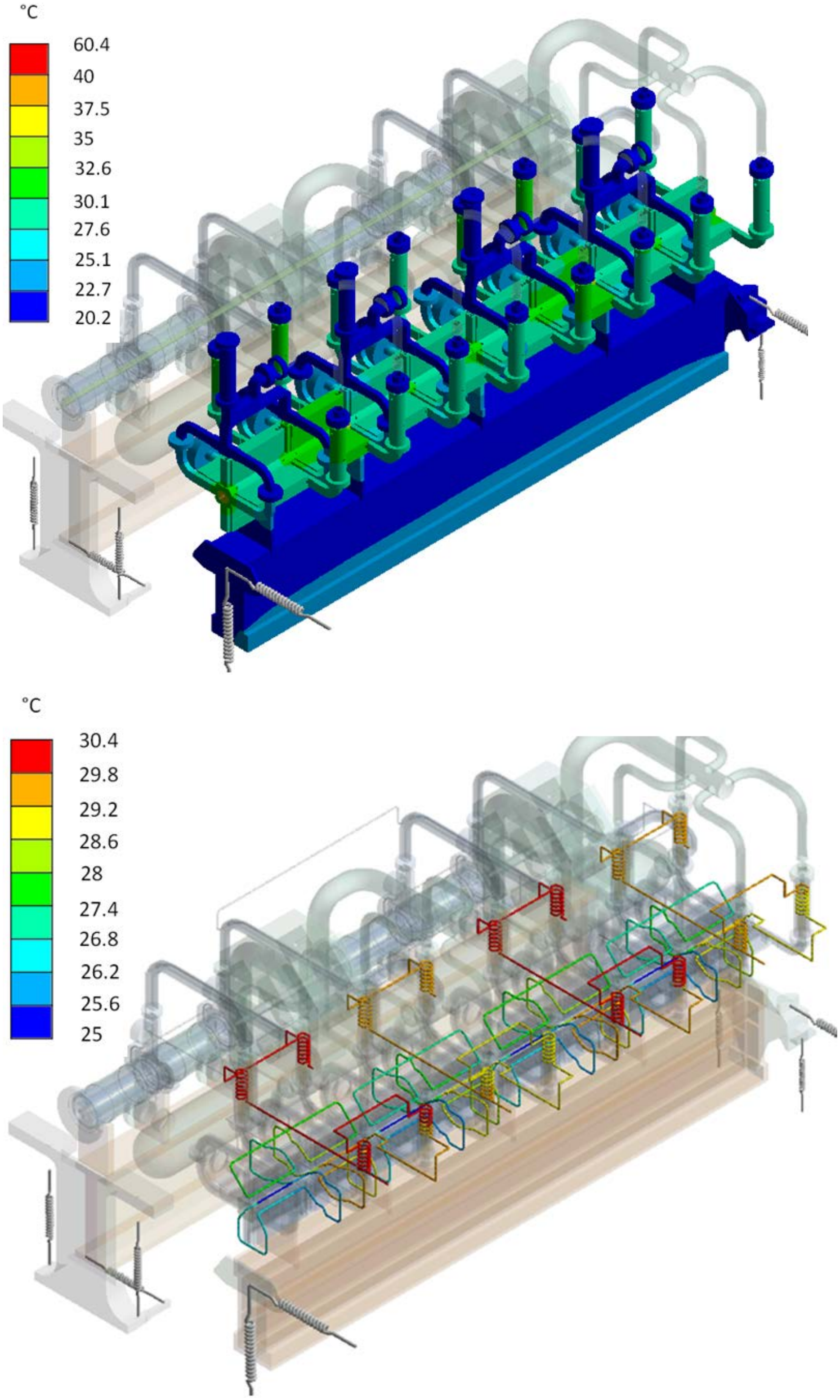

Figure 55. Calculated temperature distribution of the module for STEP 2.1 ($\dot{Q}_{AS}$ = 50%, $\dot{Q}_{ASL}$ = 50%, $\dot{V}_{SAS}$ = 0.0345 m^3/h, T_∞ = 20 °C, h_a = 38 W/m^2·°C).

6.3 STEP 3

In STEP 3 only PETS, DBQ and RFNL are heated, while the corresponding cooling system removes the generated heat. The flow rate imposed for the PETS cooling channel is the same as the CLIC baseline value (Nousiainen et al. 2010). The temperature distributions for all the substeps (different heat power, room temperature and air speed) have been measured. In this chapter the experimental results are compared to the calculated ones.

The temperature distributions of the module for STEP 3.1 (50% power) and STEP 3.2 (100% power), at the room temperature of 20 °C, are shown in Figure 56 and Figure 57, while for STEP 3.5 (50% power) and 3.6 (100 % power), at the room temperature of 40 °C, they are shown in Figure 58 and Figure 59. The temperature sensors are named in Figure 46. The numerical results are presented for three different values of the heat transfer coefficient to air (h_a = 3.8, 16 and 38 W/m^2·°C).

Since in steps 3.1 and 3.2 the temperature of the module is higher than the temperature of the air, as the theoretical heat transfer coefficient to air increases, more heat is transferred to air thus resulting in lower surface temperatures of the module. For both steps the experimental and numerical values are in agreement for a heat transfer coefficient of ~16 W/m^2·°C (Figure 60). In steps 3.5 and 3.6 the air temperature is at higher temperature and the heat flowing is flowing from the air to the module; by increasing the heat transfer coefficient in the simulation, the predicted surface temperatures are increasing. For all the heat transfer coefficients assumed, the calculated temperatures are higher than the measured ones, value 3.8 W/m^2·°C having the best correspondence between the two.

As previously described for STEP 2, it can be seen that the influence of the air speed on the measured surface temperatures of the module is negligible.

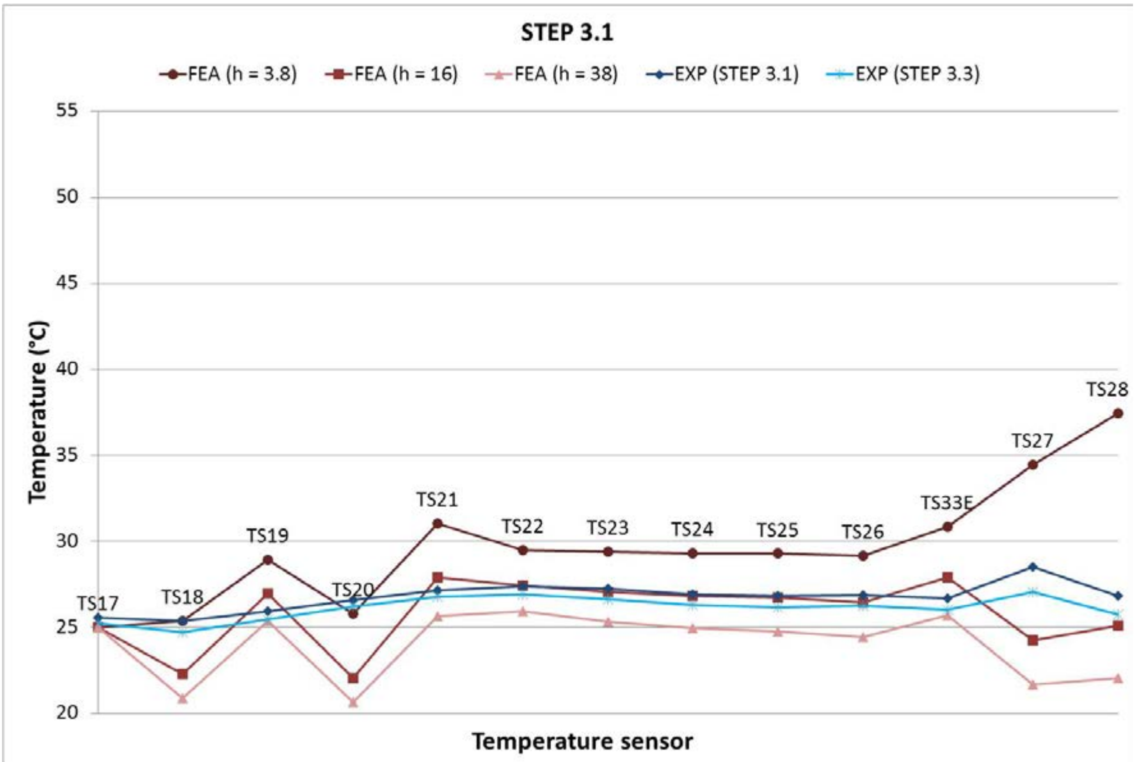

Figure 56. Temperature distribution of the module for STEP 3.1 ($\dot{Q}_{PETS}$ = 50%, $\dot{Q}_{DBQ}$ = 50%, $\dot{Q}_{RFNL}$ = 50%, $\dot{V}_{PETS}$ = 0.0374 m^3/h, T_∞ = 20 °C).

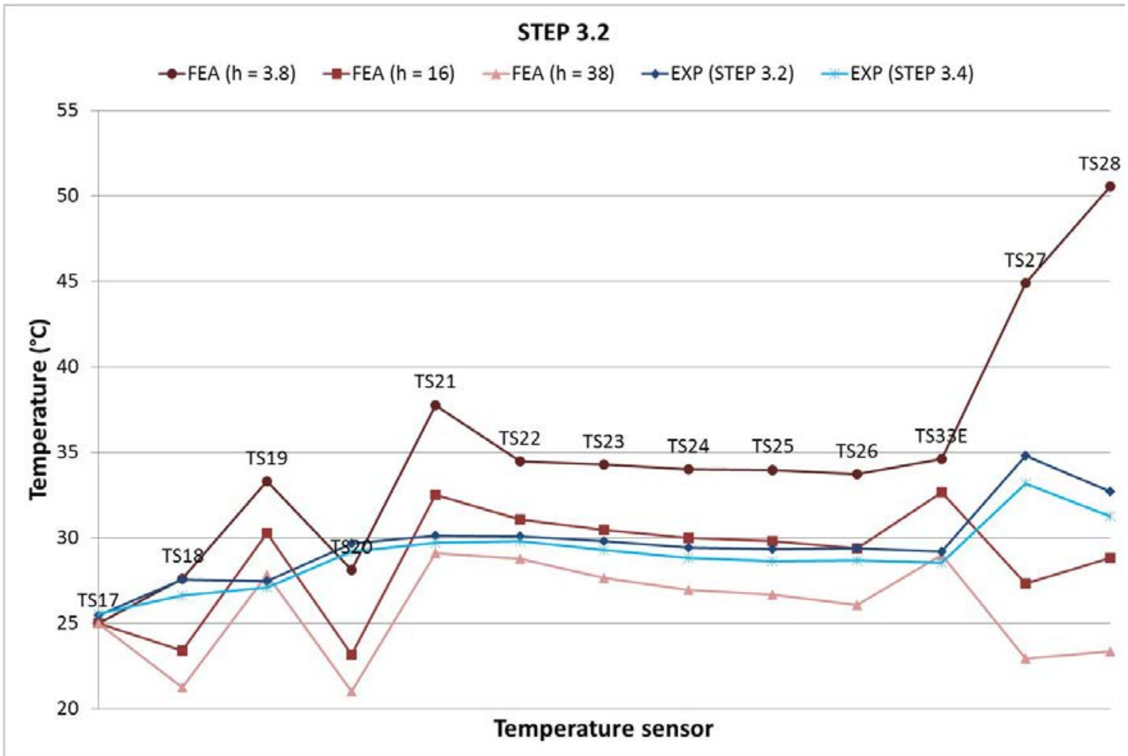

Figure 57. Temperature distribution of the module for STEP 3.2 ($\dot{Q}_{PETS}$ = 100%, $\dot{Q}_{DBQ}$ = 100%, $\dot{Q}_{RFNL}$ = 100%, $\dot{V}_{PETS}$ = 0.0374 m^3/h, T_∞ = 20 °C).

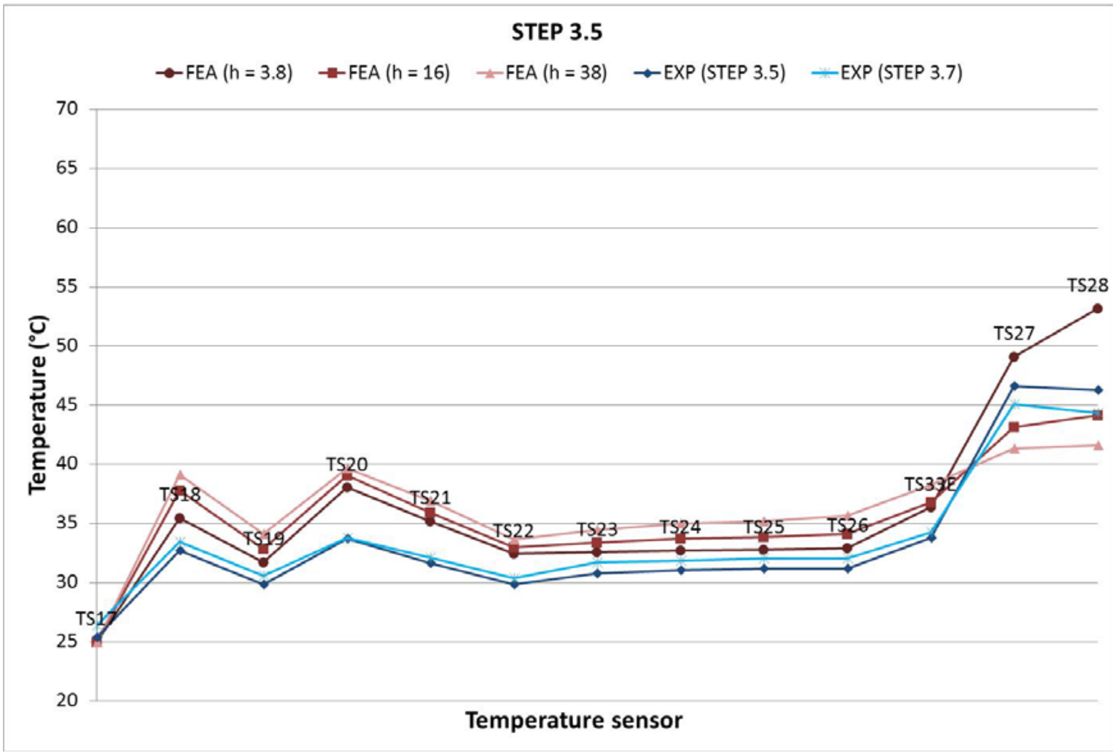

Figure 58. Temperature distribution of the module for STEP 3.5 ($\dot{Q}_{PETS}$ = 50%, $\dot{Q}_{DBQ}$ = 50%, $\dot{Q}_{RFNL}$ = 50%, $\dot{V}_{PETS}$ = 0.0374 m^3/h, T_∞ = 40 °C).

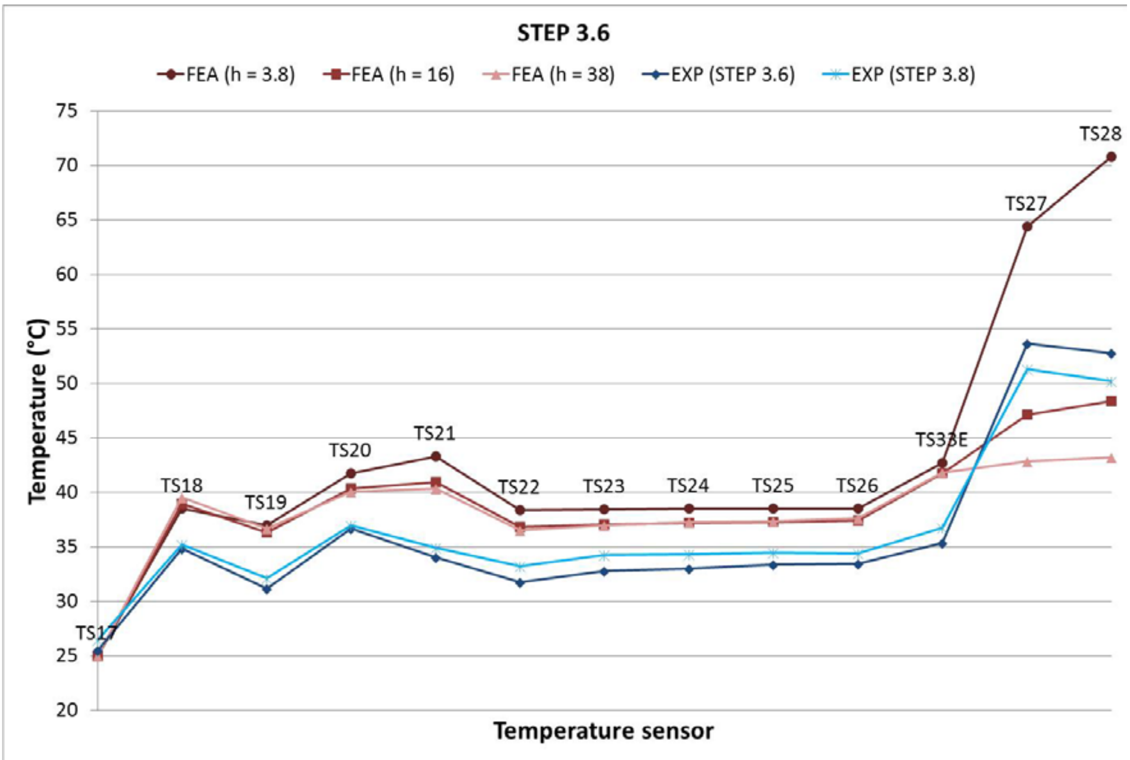

Figure 59. Temperature distribution of the module for STEP 3.6 ($\dot{Q}_{PETS}$ = 100%, $\dot{Q}_{DBQ}$ = 100%, $\dot{Q}_{RFNL}$ = 100%, $\dot{V}_{PETS}$ = 0.0374 m^3/h, T_∞ = 40 °C).

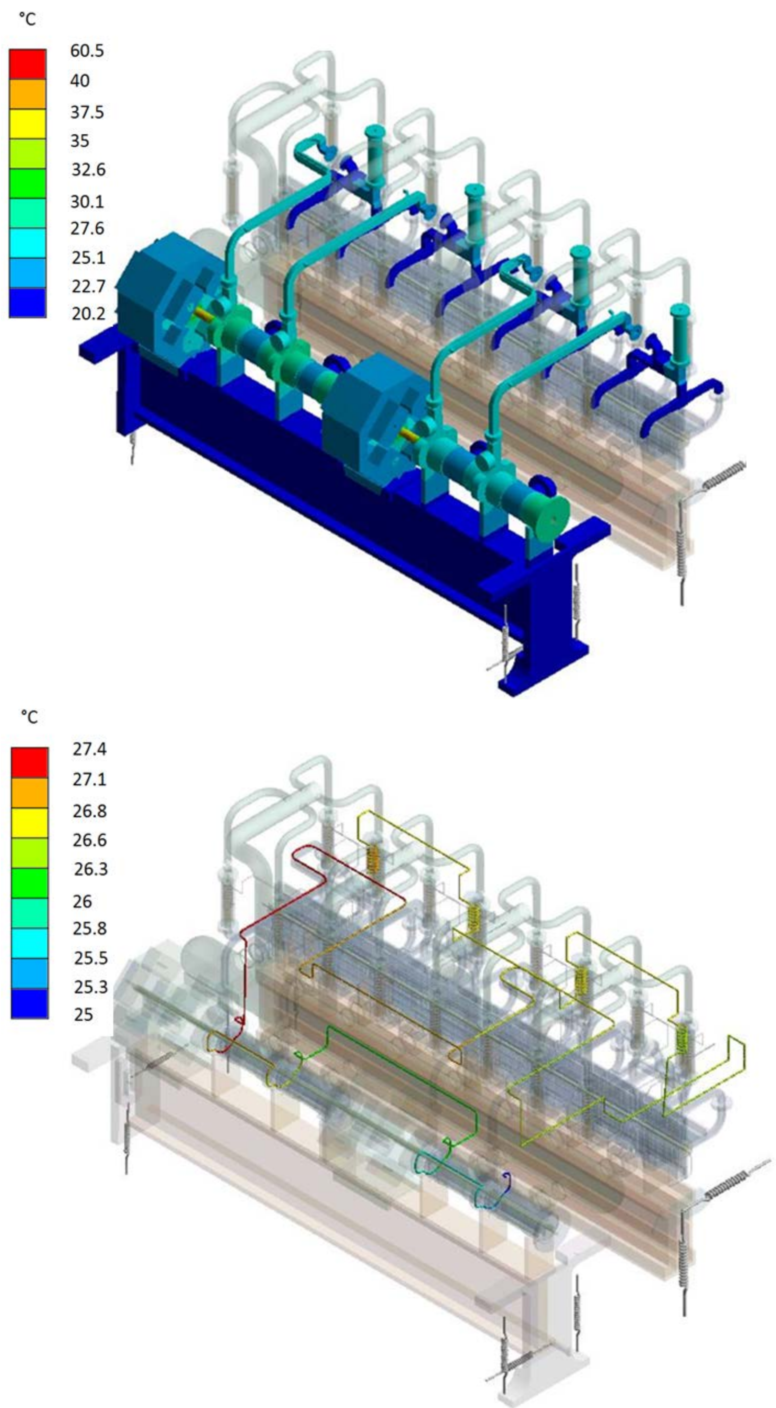

Figure 60. Calculated temperature distribution of the module for STEP 3.1 ($\dot{Q}_{PETS}$ = 50%, $\dot{Q}_{DBQ}$ = 50%, $\dot{Q}_{RFNL}$ = 50%, $\dot{V}_{PETS}$ = 0.0374 m^3/h, T_∞ = 20 °C, h_a = 16 $W/m^2 \cdot °C$).

6.4 STEP 4

In STEP 4, all the components are heated while their cooling systems are active. As in STEP 2, only the substeps 4.1, 4.3 and 4.5 with 50% of the nominal heat power have been completed because of an overheating AS heater. The remaining steps will be done when the new heater is delivered. In STEP 4, the CLIC baseline values have been used for the flow rates of the cooling channels. The temperature of the module is calculated for steps 4.1 (50% power, 20 °C room temperature) and 4.5 (50% power, 40 °C room temperature) using heat transfer coefficients based on the results from steps 2 and 3. For STEP 4.1 the values used are h_a = 38 W/m^2·°C for MB side and h_a = 16 W/m^2·°C for DB side. For STEP 4.5 heat transfer coefficient h_a = 3.8W/m^2·°C is used for both sides. The surfaces selected for the different coefficients are seen in Figure 61.

The measured and predicted temperature distributions of the module for STEP 4.1 and STEP 4.5 are presented in Figure 62 and Figure 63. As seen previously, at 20 °C room temperature, the calculated results correspond well to the measured ones, while at 40 °C the calculated temperatures are higher than the measured ones. The predicted results for STEP 4.1 are also shown in Figure 64.

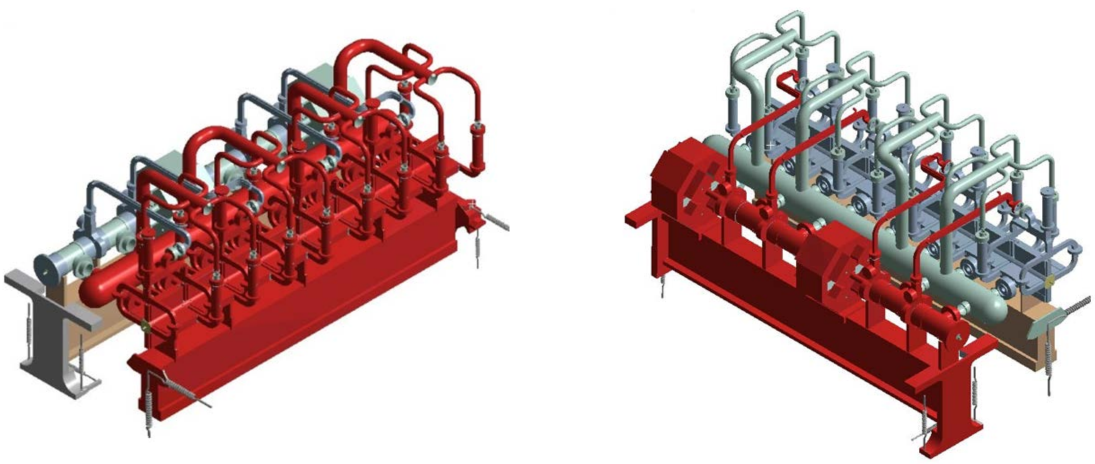

Figure 61. The surfaces for the transfer coefficients to air for MB (left) and DB (right) sides for STEP 4.

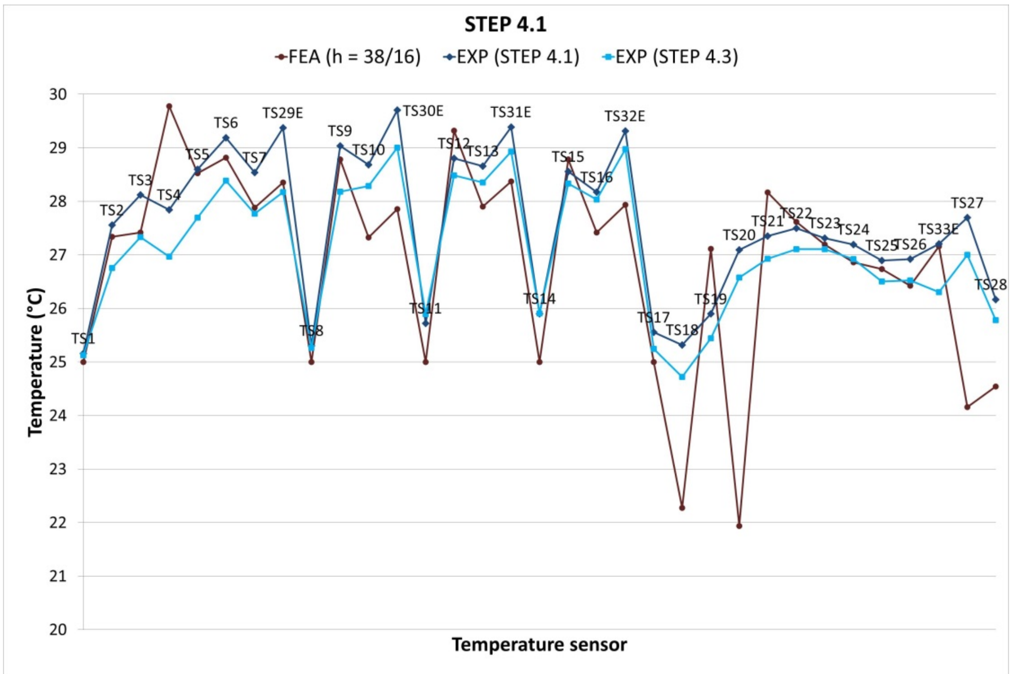

Figure 62. Temperature distribution of the module for STEP 4.1 ($\dot{Q}_{AS}$ = 50%, $\dot{Q}_{ASL}$ = 50%, $\dot{Q}_{PETS}$ = 50%, $\dot{Q}_{DBQ}$=50%, $\dot{Q}_{RFNL}$=50%, $\dot{V}_{SAS}$ = 0.066 m^3/h, $\dot{V}_{PETS}$ = 0.0374 m^3/h, T_∞ = 20 °C).

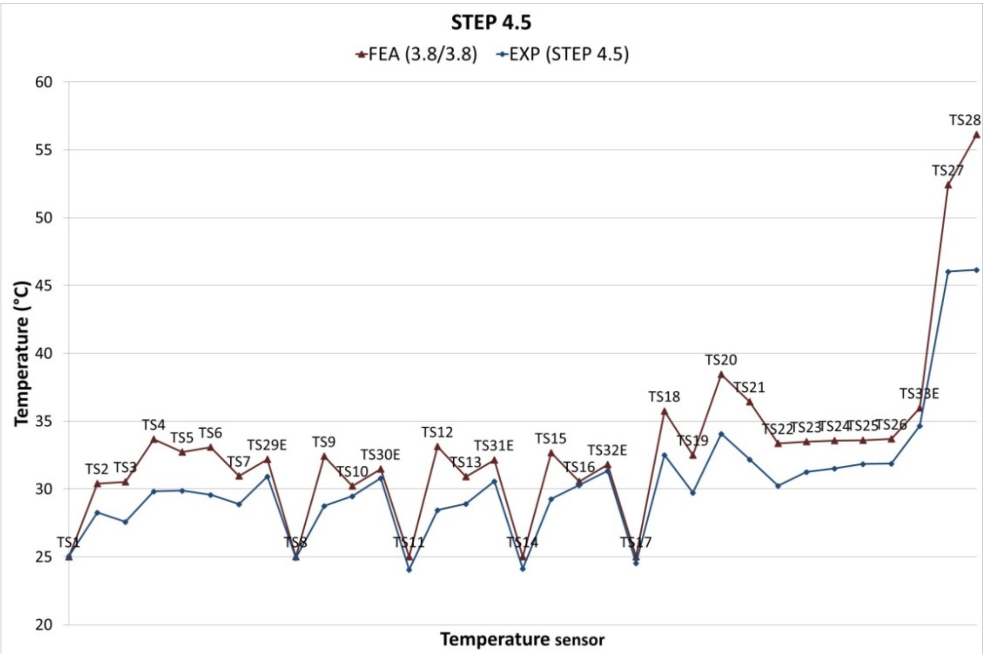

Figure 63. Temperature distribution of the module for STEP 4.5 ($\dot{Q}_{AS}$ = 50%, $\dot{Q}_{ASL}$ = 50%, $\dot{Q}_{PETS}$ = 50%, $\dot{Q}_{DBQ}$=50%, $\dot{Q}_{RFNL}$=50%, $\dot{V}_{SAS}$ = 0.066 m^3/h, $\dot{V}_{PETS}$ = 0.0374 m^3/h, T_∞ = 40 °C).

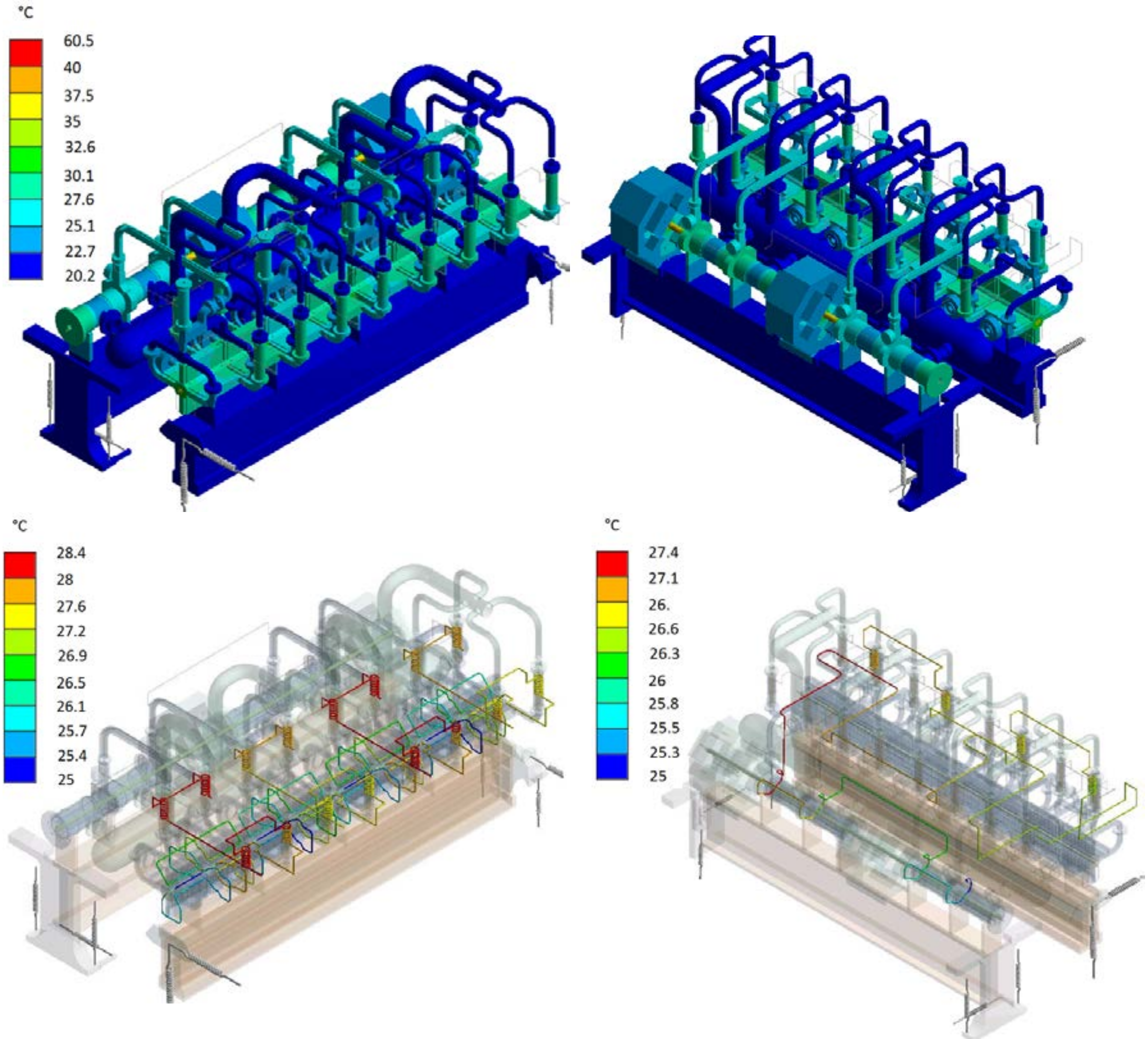

Figure 64. Calculated temperature distribution of the module for STEP 4.1 ($\dot{Q}_{AS}$ = 50%, $\dot{Q}_{ASL}$ = 50%, $\dot{Q}_{PETS}$ = 50%, $\dot{Q}_{DBQ}$=50%, $\dot{Q}_{RFNL}$=50%, $\dot{V}_{SAS}$ = 0.066 m^3/h, $\dot{V}_{PETS}$ = 0.0374 m^3/h, T_∞ = 20 °C).

6.5 Vacuum

The predicted effect of the vacuum load on the structural behaviour of the module is presented in Figure 65. It is worth noting that the RF network waveguides are pushed towards the hybrids due to the vacuum load; the bigger the bending stiffness of the waveguides, the lower the corresponding displacement.

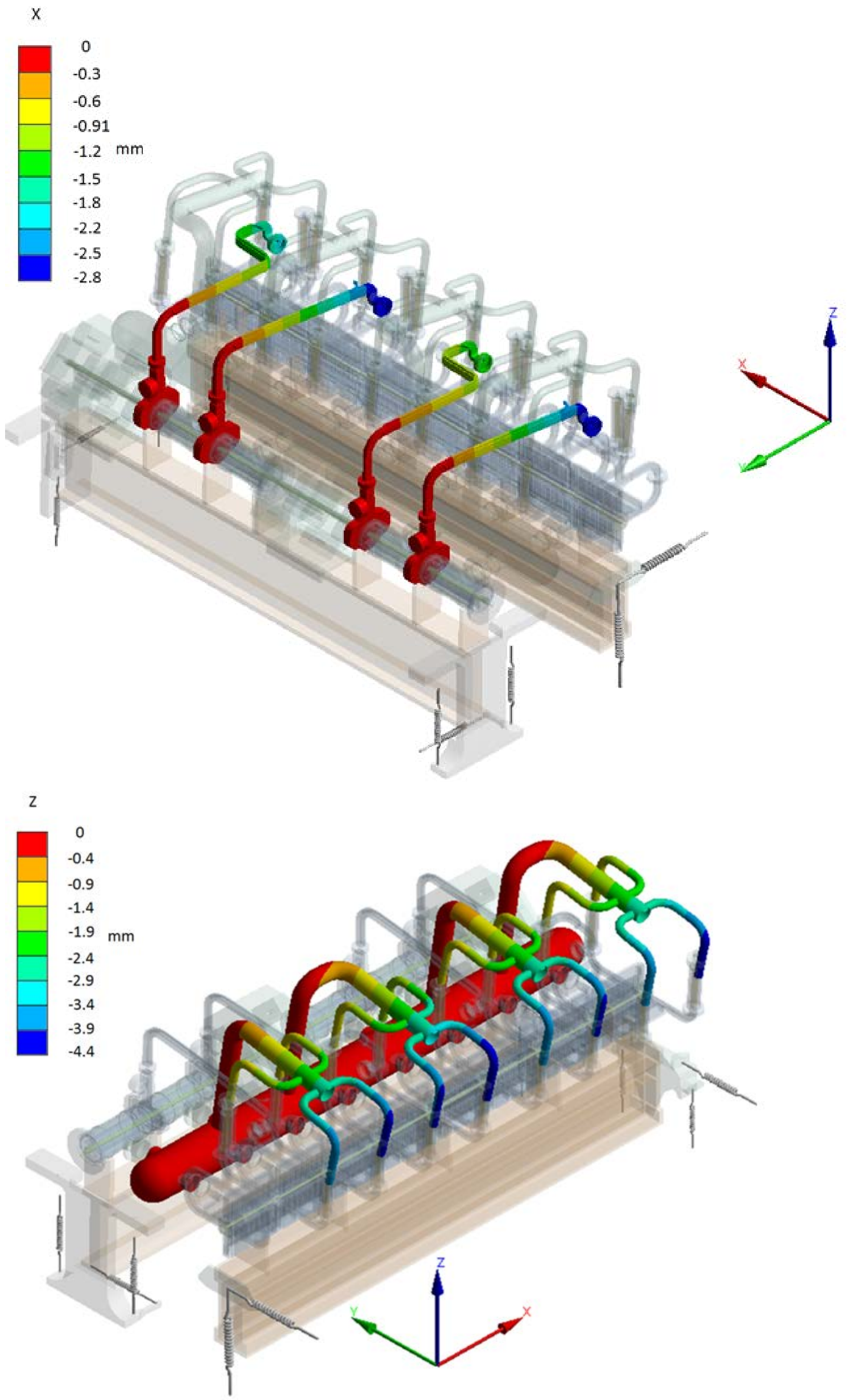

Figure 65. The calculated deformations induced by the vacuum load.

7 CONCLUSIONS AND FUTURE STEPS

The luminosity goal of CLIC imposes micron level stability requirements on its two-meter repetitive elements, the CLIC modules, constituting the two main linacs. Thermal loads due to RF power dissipated inside the modules produce deformations affecting the alignment of the linacs and therefore the resulting luminosity. Other external loads, such as vacuum and gravity, give additional contributions to the final misalignments in and between different elements.

The first CLIC prototype module has been assembled in a dedicated laboratory and a thermal test program has been started to study its thermo-mechanical behaviour under different operating conditions. In parallel a finite elements model of the module has been realized. The results from the experimental tests have been compared to the calculated ones. The comparison shows that the experimental and numerical results are in good agreement both for the thermal behaviour of the module and for the resulting misalignments.

In STEP 1, where only the ambient temperature was varied, the calculated displacements of the beam axes in three directions, corresponding to an increase of temperature of 10 °C, were compared to the experimental results. Taken into account the tolerances of the measurement devices, the predicted and the measured displacements were in good agreement. In STEP 2, AS and CL were heated; the surface temperature measurements were done only for the substeps with 50% of the AS power dissipation. At the room temperature of 20 °C, the correspondence between the numerical and measured surface temperatures was found for a heat transfer coefficient to air of 38 $W/m^2\cdot°C$, while at the room temperature of 40 °C they were in agreement using a theoretical heat transfer coefficient of 3.8 $W/m^2\cdot°C$. According to the measurements changing the air speed had negligible effect on the surface temperatures. In STEP 3, PETS, DBQ and RFNL were heated; the measurements were completed for all the substeps. As for STEP 2, the numerical results were calculated using different heat transfer coefficients. At room temperature of 20 °C, the results were in agreement for a heat transfer coefficient of 16 $W/m^2\cdot°C$, while at room temperature of 40 °C the correspondence was found for a value 3.8 $W/m^2 \cdot °C$. The measured surface temperatures were not affected by changing the air speed. In STEP 4 all the components were heated and water cooled; only the substeps with 50% power were completed. For the numerical calculation of STEP 4.1, two different heat transfer coefficients to air were imposed on the module based on the results from previous steps: for MB side a heat transfer coefficient of 38 $W/m^2 \cdot °C$ was used whereas for DB side the value used was 16 $W/m^2 \cdot °C$. For STEP 4.5, at 40 °C room temperature, the value used was 3.8 $W/m^2 \cdot °C$ for both sides. The calculated surface temperatures were similar to the measured ones in both steps.

In the next future a fluid-dynamic model of the laboratory, where the module is installed, will be developed. Knowledge from this study will be propagated back to the finite elements simulation of the module.

.

8 REFERENCES

BOA Group (2010) Metal Bellows Consultant Issue 27.2-UK. http://pdf.directindustry.com/pdf/boa/metal-bellows/26032-121884.html [1.10.2012]

Witzenmann (2010) HYDRA Stainless Steel Bellows. http://www.witzenmann.in/download/Manual%20of%20metal%20bellows_0441e%20S%2095-115_2_04_10_20_web.pdf [1.10.2012]

Cengel YA (2002). Heat Transfer: A Practical Approach. New York: McGraw-Hill.

CERN (2013) About CERN. http://home.web.cern.ch/about. [1.4.2013]

CERN (2013) Member states. http://home.web.cern.ch/about/member-states. [1.4.2013]

CERN (2010) Physics for health. http://physics-for-health.web.cern.ch/physics-for-health. [1.4.2013]

Ellis JR (2000) Physics Goals of the Next Century at CERN. CERN-TH-2000-050.

Ellis JR & Wilson I (2000) New Physics with the Compact Linear Collider. CLIC-Note-466.

Geschonke G (2010) The Next Energy-Frontier Accelerator a Linear e+e- Collider?. CERN-OPEN-2010-007. CLIC-Note-807.

Gudkov D (2013) Description of the first CLIC Two-Beam Module prototype Type 0.

Griffet et al (2012) Strategy and validation of fiducialisation for the pre-alignment of CLIC components. The International Particle Accelerator Conference, May 2012, New Orleans, USA.

Holman JP (2010) Heat Transfer. New York: McGraw-Hill.

Kothandaraman CP (2006) Fundamentals of Heat and Mass Transfer. New Delhi: New Age International (P) Ltd., Publishers.

Nousiainen et. al (2010) Studies on the Thermo-Mechanical behaviour of the CLIC Two-Beam Module. Linear Accelerator Conference, September 2010, Tsukuba, Japan.

Rohsenow et al. (1998) Handbook of Heat Transfer. New York: McGraw-Hill.

Rossi et al. (2012) Study of the Thermo-Mechanical Behaviour of the CLIC Two-Beam Modules.

Stapnes et al. (2012) A Multi-TeV linear collider based on CLIC technology: CLIC Conceptual Design Report. CERN 2012-007.

Samoshkin et al. (2011) CLIC Two-Beam Module for the CLIC Conceptual Design and Related Experimental Program. TUPC008, IPAC2011, San Sebastian, Spain.